THE JOURNAL OF PHYSICAL CHEMISTRY B
A JOURNAL OF THE AMERICAN CHEMICAL SOCIETY

pubs.acs.org/JPCB

Article

Ion Transport through Permselective Nanochannels of 2D-Covalent Organic Frameworks: Insights from Nonequilibrium Atomistic MD Simulations

Sai Manoj Gali,[#] Quentin Thomas,[#] Nicolas Karageorgos, Nicolas Rolland, Pascal Damman,* and David Beljonne*

Cite This: *J. Phys. Chem. B* 2026, 130, 5775−5790

Read Online

ACCESS | Metrics & More | Article Recommendations | Supporting Information

ABSTRACT: Covalent organic frameworks (COFs), with their long-range crystallinity, rigidity, and highly tunable molecular porosity, are evolving as promising next-generation ion-permselective membranes for ion separation, reverse electrodialysis, and osmotic energy conversion. Herein, we employ steady-state nonequilibrium molecular dynamics (SS-NEMD) simulations to accurately and realistically describe the concentration-driven ion permeation process through functionalized and charged COF membranes and gain a fundamental understanding of the factors governing the ion transport in COFs. To this end, we model the diffusion of K^+ and Cl^- ions through the COF membranes that are suspended in aqueous electrolyte and are decorated with either propanesulfonic acid or sulfonic acid-terminated oligo(n)-ethylene glycol chains. We systematically vary the percentage of charged groups present within the nanoporous domains and demonstrate that the ion permeation, and thus the ion selectivity in these systems, depends on the concentration gradient of ions across the membrane, as modulated by the presence and degree/percentage of charged groups within the COF membranes. We further demonstrate that COF membranes decorated with charged oligo(n)-ethylene glycol chains show enhanced ion selectivity ratios, even when partially charged, reaching efficiencies of around 99% when compared to COFs with alkylated chains that show efficiencies of around 80%.

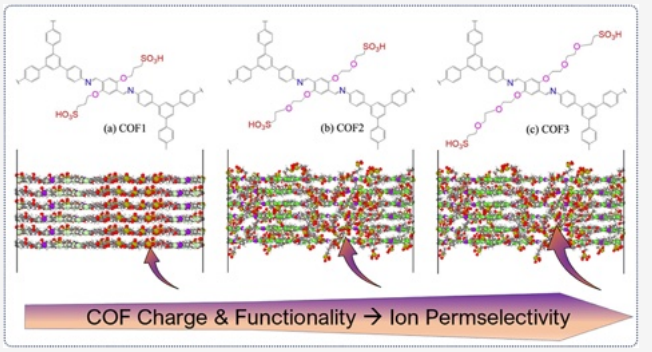

1. INTRODUCTION

Covalent organic frameworks (COFs), offering a large versatility in chemical building blocks, are an emerging class of layered two-dimensional crystalline semiconductors that combine the excellent optoelectronic properties of their conjugated polymer backbones with permanent nanoporosity, enabling the design of host−guest interactions to realize multifunctional materials.[1−4] Seminal studies by Yaghi et al.,[5,6] demonstrating "one-pot" synthesis of two-dimensional (2D)-COFs with long-range crystallinity, high thermal stability, low densities, and permanent "molecular" porosity, unlocked a scientific fervor for these novel classes of organic materials that led to the development of semiconducting photoactive 2D-COFs with tunable optoelectronic properties[7−11] and exceptional charge carrier mobilities.[12] Subsequent academic interest in 2D-COFs also led to additional studies exploring their potential applications in gas storage, energy storage,[13−16] and catalysis.[17] Thanks to their nanoporous structure, atomically smooth channels and tailor-made pore sizes,[18,19] COFs offer an ideal framework for metal ions (Li^+, Na^+, K^+, Zn^{2+}...)[20−26] and proton[27] storage via redox reactions, especially in secondary ion batteries or as efficient electrode skins with high anion-transport capability and selectivity.[28] Of late, 2D-COFs are also emerging as promising ion-permselective membranes for monovalent ion separation,[29] reverse electrodialysis,[30] and blue energy harvesting,[31−35] wherein the surface charge inside the COF nanochannels allows for a selective passage of electrolyte ions, in accordance with the charge polarity, thus separating the electrolyte ions with different concentrations. Topical academic investigations demonstrated the explorative application of COF membranes in harvesting the osmotic energy using reverse electrodialysis, where the salinity gradient between seawater and river water enables the COF permselective membranes to selectively transport cations and anions between the electrodes.[36−38] Although other emerging 2D materials like graphene oxide,[39,40] MoS_2,[41] Mxene,[42,43] and

Received: March 6, 2026
Revised: May 19, 2026
Accepted: May 20, 2026
Published: May 26, 2026

https://doi.org/10.1021/acs.jpcb.6c01511
J. Phys. Chem. B 2026, 130, 5775−5790

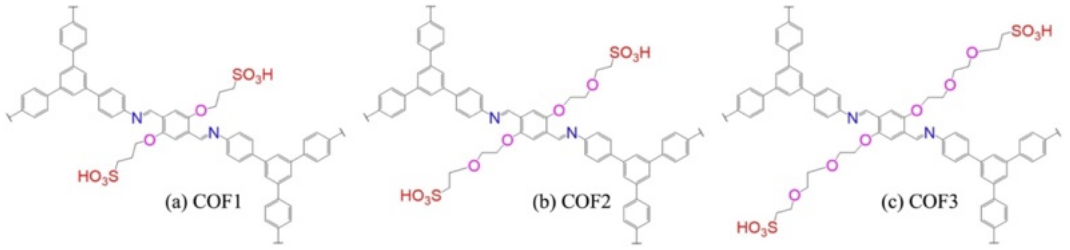

Figure 1. Schematic representation of the functional COF variants employed in this work; (a) left: propanesulfonic acid-functionalized COF-DT, aka COF1; (b) middle: sulfonic acid-terminated 2-ethylene glycol, aka COF2; and (c) right: sulfonic acid-terminated 3-ethylene glycol, aka COF3.

boron nitride[44] were also used as ion-transporting membranes, ion flux in these systems is dictated by percolation channels, thus making these 2D membranes less efficient for osmotic energy harvesting.[45,46] With high crystalline order and spatially separated pathways for charge and ion transport, properly designed and functionalized COFs can combine a large accessible surface area for ion storage and precise molecular/ion transport.[47−53]

Recently, Wang et al. demonstrated efficient separation of monovalent cations by employing functionalized TpPa-2D-COF membranes constituted from 1,3,5-triformylphloroglucinol (Tp) and 2,5-diaminophenyl (Pa) groups that are functionalized to contain either (i) phosphonic acid groups (Pa−PO3H2), (ii) sulfonic acid groups (Pa−SO_3H), or (iii) benzoic acid groups (Pa−CO2H).[29] From diffusion dynamics driven by concentration gradients (with aqueous salt solutions of RbCl, KCl, NaCl, and LiCl mixtures placed on one side of the TpPa-2D-COF membranes, hitherto referred to as the feed side, and deionized water placed on the other side of the COF membranes, hitherto referred to as the permeate side), they demonstrated that the functionalized TpPa-2D-COF membranes not only permeated the monovalent cations screening the anion counterparts but also showed efficient ion selectivity separating the cations from discrete binary mixtures with different permeation rates.

In another study, Cao et al. used COF-DT membranes based on 1,3,5-tris(4-aminophenyl)benzene and 2,5-dihydroxy-1,4-benzenedicarboxaldehyde (DHBDA) as COF building blocks for osmotic energy conversion. There, the DHBDA unit of COF-DT was postsynthetically functionalized to contain either propanesulfonic acid, resulting in COF-SO_3H, or (propyl)trimethylammonium, resulting in COF-QA.[54] Ion transport through these functionalized COF membranes that were sandwiched between two electrochemical cells containing KCl electrolyte was investigated through the ion diffusion with concentration gradients, similar to the approach adopted by Wang et al.[29] Cao et al. demonstrated that the negatively (positively) charged COF-SO_3H (COF-QA) membranes selectively passed K^+ (Cl^-) ions resulting in the separation of K^+ (Cl^-) and Cl^- (K^+) ions across the COF-DT membranes, building a chemical potential gradient due to the different concentrations of cations and anions and therefore to osmotic currents. Furthermore, Cao et al. showed that the ionic conductivities of K^+ (Cl^-) ions improved significantly by increasing the number of negatively (positively) charged functional units (hitherto referred to as group density) on the COF-SO_3H (COF-QA) membranes. In addition, a decrease in the ionic conductivities of cations/anions when increasing the thickness of the COF was observed in these studies, which was partly attributed to the effect of transport resistance offered by thicker COF membranes (as also previously observed in other systems[55−57]).

Interestingly, both of the above-mentioned works by Wang et al.[29] and Cao et al.[54] show that different COF membranes (TpPa-COF and COF-DT), when decorated with similar (acidic) functional groups, behave similarly in terms of their applicability in concentration-driven ion separation and/or ion conductivity applications. This clearly indicates the role of the nature and the density of functional groups on the resulting ion selectivity and/or permselectivity of functional 2D-COF membranes.

At this juncture, as the functional 2D-COF membranes are evolving as promising candidates for ion selectivity and/or blue energy (reverse osmosis) applications,[29,36−38,54] there is thus an implicit need of a robust theoretical framework to not only describe the "steady-state" concentration-driven ion transport process in these functionalized COF membranes, but also derive COF structure−ion transport property relationships to improve the efficiency of COF membranes toward enhanced ion selectivity ratios and/or osmotic energy conversion. Although the work of Cao et al.[54] was supported by atomistic molecular dynamics (MD) simulations providing a qualitative agreement with experimental observations, their simulation protocol starts with an initial differential concentration gradient between feed and permeate sides of the COF membrane, which then evolves continuously, with time, toward the equilibrium state. Recent studies employing MD simulations to study ion transport in functional COF membranes, either to model the transport of mono/divalent cations[58] and anions[59] in functional COF membranes or to understand the water transport in functionalized COF nanochannels,[60,61] also invoke similar out-of-equilibrium protocols, where a concentration gradient of ions is established between the feed and permeate sides of the membranes at the start of the MD simulations. However, in these simulations, as the simulation progresses in time, the concentration gradient decreases, taking the nonequilibrium system toward equilibrium where the initially set concentration gradient reaches zero. Consequently, the ionic fluxes obtained with such simulation protocols continuously change during the simulation due to the temporal evolution/variation of the concentration gradient between the feed and permeate sides and may not reflect a "steady-state" concentration gradient and/or "steady-state" nonequilibrium condition making it difficult to obtain reliable diffusion coefficients.

Therefore, the description of ion permeation through (functionalized) COF membranes calls for simulations that are to be performed under a nonequilibrium steady state and continuous flow of ions across the COF membranes while maintaining a constant concentration gradient between the

https://doi.org/10.1021/acs.jpcb.6c01511
J. Phys. Chem. B 2026, 130, 5775−5790

feed and permeate regions of the COF membranes throughout the simulation time.

To this end, we deploy a concentration-driven "steady-state nonequilibrium" molecular dynamics formalism,[62] hitherto referred to as SS-NEMD, to realistically simulate the out-of-equilibrium ion diffusivity process through functionalized and charged COF membranes (containing a finite array of COF layers). Herein, a constant concentration gradient of ions between the feed and permeate sides of the COF membrane is temporally preserved throughout the MD simulations and the permeation of ions through functionalized and charged COF membranes is evaluated to assess the impact of the concentration gradient between the feed and permeate sides and the nature of functional groups decorating the COF porous domains.

Accordingly, we consider the COF-DT membrane functionalized with (propane) sulfonic acid as a model system, based on the recent work of Cao et al.,[54] resulting in COF-SO_3H, hitherto referred to as COF1, see Figure 1(a) for a schematic representation and Supporting Information (SI) Figure S1 for a schematic representation of COF-DT. Considering an aqueous KCl solution, ion permeation of K^+ and Cl- ions through the COF pores/membranes was studied as a function of the density (percentage) of charged groups present within the nanoporous domains and as a function of (i) the total molar concentration of the ions in the simulation cell and (ii) the concentration gradient between the feed and permeate sides of the COF membranes. In extension, the influence of the nature and length of side chains containing the sulfonic acid groups on the resultant ionic fluxes was also studied by considering two more COF-DT variants in addition to COF1, wherein the propane-sulfonic acid group is substituted with sulfonic acid-terminated oligo(n)-ethylene glycol; n = 2 and 3, hitherto referred to as COF2 and COF3, respectively (see Figure 1(b) and (c), respectively, for schematic representation). Our choice of selecting oligo(n)-ethylene glycol toward COF functionalization is driven by two factors: (i) the fact that such functionalization is experimentally feasible via the Williamson ether reaction using poly(ethylene oxide) halides; and (ii) that oligo(n)-ethylene glycol chains with varying chain lengths (n = 2, 3, 4) provide an easy and alternate way to modulate the effective pore size of the COF membranes (in addition to that reported by Wang et al.,[29] where TpPa-COF membranes with different pore sizes were synthesized by changing the nature and size of diamine monomers constituting the COF building block). In addition, the oligo(n)-ethylene glycols could provide additional flexibility and higher polarity that can potentially enhance the ion selectivity in addition to providing better stability in an aqueous medium due to their hydrophilic nature.[63] We also compare the ion permeation in COF1 membranes using both SS-NEMD and nonequilibrium MD simulations. In the latter case, the simulation boxes containing the COF1 membranes were sealed by a graphene wall and K^+ and Cl^- ions were placed only on the feed side of the COF1 membranes while the permeate side contained no ions, similar to the work of Cao et al.,[54] hitherto referred to as "slab-MD". We demonstrate that the positive ion flux, diffusivity, and the corresponding ion selectivity and/or ion transference number in the (negatively charged) COF1 membranes are indeed related to (i) the percentage of charged -SO_3H groups in COF nanochannels and (ii) the nature and length of side chains containing the charged groups. Therefore, through this study, we not only describe the steady-state out-of-equilibrium ion permeation process through (charged) COF membranes accurately and realistically, but we also give an insight into the structure-ion transport property relationship by comparing the behavior of three COF variants (alkylated vs glycolated). Our analysis provides a comprehensive understanding of the complex ion transport mechanisms down to the nanometer scale, which hopefully can guide experimental synthesis toward functional COF variants that can be actively used either as ion permselective membranes or in osmotic/blue energy generators.

2. COMPUTATIONAL METHODOLOGY

2.1. Potential Energy Scan Calculations

DFT-based Potential Energy Surface (PES) calculations were performed to determine the most stable interlayer stacking mode of the COF systems in their bulk forms. These calculations were performed with the projector-augmented wave (PAW) basis set, as implemented in the VASP code, treating the exchange and correlation effects at the Perdew−Burke−Ernzerhof (PBE) level.[64,65] Dispersion forces by Grimme correction (PBE+D3)[66] were incorporated to account for vdW interactions between the COF layers. The kinetic energy cutoff was set to 500 eV using a Monkhorst−Pack sampling of 3 × 3 × 1 for monolayers and 3 × 3 × 3 for bulk samples to account for the Brillouin zone integration for all geometry optimizations and the subsequent SCF calculations, at the GGA/PBE level of theory. For 2D-COF monolayers, vacuum spacing was set to 30 Å to avoid interactions with periodic images. All the geometries were fully optimized, and the DFT-optimized energies were recorded to determine the most stable geometry/stacking mode with the lowest relative energy. Potential Energy Surface (PES) calculations indicate that the most stable stacking mode of COF1 corresponds to Serrated-X stacking ([100] direction) with an interlayer shift of ≈0.075 times the unit-cell ***a***-axis length (with a corresponding lateral displacement of 2.7 Å), see Supporting Information Section S1 for a detailed description. In comparison, the cofacial (AA) stacking mode is relatively high in energy (by ∼3 eV), meaning that such a stacking mode is energetically not favorable. See Supporting Information Figure S2a for details. PES calculations performed on unfunctionalized COF-DT membranes also reveal similar trends (Supporting Information Figure S3), indicating that the functionalization of COF-DT membranes with the propanesulfonic acid group (COF1) does not significantly alter the interlayer stacking mode. Indeed, previous investigations indicate that the interlayer stacking mode in 2D-COFs, showing either cofacial[7−10,67,68] or slip-stacked[69−73] modes, comes down to the interplay between competing Coulombic and vdW interlayer interactions[74−77] between the COF building blocks. Subsequently, density-derived electrostatic charges (DDEC06)[78−81] were extracted for COF monolayers and the respective COF monolayers along with their corresponding DDEC06 charges were introduced into Molecular Mechanics force field (MM) calculations performed with the DREIDING[82] force field using the Forcite module as implemented in the BIOVIA Material Studio (2022) software; electrostatic interactions were treated with the particle mesh Ewald (PME) summation to account for long-range electrostatic interactions. Different stacking modes (Inclined-X/XY and Serrated-X/XY) were prepared following the procedure explained in Supporting

https://doi.org/10.1021/acs.jpcb.6c01511
J. Phys. Chem. B 2026, 130, 5775−5790

Information Section S1 and potential energy scan calculations were performed to determine the energetically stable interlayer stacking mode. MM potential energy scan calculations also indicate that the Serrated-X stacking mode ([100] direction) with an interlayer shift of 0.075 times the unit-cell ***a***-axis parameter (corresponding displacement of 2.7 Å) is the most stable interlayer stacking mode. Overall, the results of our MM potential energy scan calculations are in good qualitative agreement with those obtained from DFT calculations. Given the high rigidity of the COF structure and the frozen "backbone" atoms invoked during the SS-NEMD simulations (vide infra), the force field to replicate the interlayer stacking modes of COF layers is less important, provided that it describes well the interactions with ions and water. Interestingly, these COF layers in their energetically stable Serrated-X stacking mode show an identical pXRD pattern to that of the cofacial (eclipsed, AA) stacking mode (the latter being higher in energy), with prominent diffraction peaks at 2.8°, 4.9°, 5.6°, and 7.4° (see Figure S4 for details) in line with those reported by Cao et al.[54] As the pXRD patterns of the cofacial stacking mode in COFs can be similar to that of the serrated stacking mode, determination of the stable interlayer conformation of the COF membranes from PES calculations is, therefore, extremely important as a change in the interlayer stacking mode can not only alter the electronic structure of the COFs, as recently demonstrated,[83] but can also vary the size/diameter of the nanoporous COF domains and thus can potentially alter the solvent/ion-accessible nanoporous volume of the COF membranes,[60] both of which can in turn modulate the ion flux and/or ion selectivity ratios.

2.2. Molecular Dynamics Simulations

All atomistic MD simulations were performed with the LAMMPS package.[84] COF membranes were constructed from monolayers replicated 4 × 4 × 6 times such that the simulation box contains 4 nanoporous domains and 6 layers replicating the energetically stable Serrated-X ([100]) stacking mode as determined by both DFT and Forcite-MM calculations, and these membranes were positioned in the center of the simulation cell approximately 6.27 × 7.24 × 15.0 nm^3 in size. Explicit water molecules and K^+/Cl^- electrolyte ions were added such that the initial density of the system is around 1 g/cm^3 and that the total molar concentration of ions in the simulation cell is between 0.2 M and/or 0.4 M (similar to the works of Wang et al.[29] and Cao et al.[54]), taking the total number of atoms used in the simulation to approximately 67000. For negatively charged COF membranes, additional K^+ ions were added appropriately to counter the (negative) SO_3^- units decorating the COF membrane and to ensure charge neutrality in the simulation box. An initial minimization step is performed followed by an equilibration step of 8 ns, consisting of 2 ns of simulation run in the NVT ensemble, successively followed by 4 ns of simulation run in the NPT ensemble to accommodate density changes if any and by an additional 2 ns of simulations in the NVT ensemble. Subsequently, MD simulations were performed for a minimum of 60 ns for the production run, following the initial thermodynamic equilibration. Periodic boundary conditions were applied in all three directions, and the temperature was set to 298 K using the Nosé-Hoover thermostat. The DREIDING[82] all-atom force field was used to describe the COF membranes with charges extracted from the DFT/GGA/DDEC06[78−81] method, while the force field parameters for K^+/Cl^- ions and for the the SPC/E water model were taken from the literature.[85−87] In order to prevent the drifting of COF membranes in the *z*-direction of the simulation box due to the presence of charged functional groups and/or the presence of counterions in the vicinity of COF charges within the nanoporous domains and/or to the concentration gradient, the heavy atoms pertaining to the COF skeleton were frozen after the minimization step while the atoms of the functionalized units were allowed to move. The particle−particle particle-mesh (PPPM) solver was employed to calculate the long-range electrostatic interaction, with a cutoff of 1.2 nm for the separation of the direct and reciprocal space summation. The cutoff distance for the van der Waals interaction was set to 1.2 nm, and the parameters of the Lennard-Jones potential for the cross-interactions between nonbonded atoms were obtained from the Lorentz−Berthelot combination rule.

Diffusive transport of K^+ and Cl^- ions in single-component KCl solutions through the functionalized (negatively charged) COF membranes was studied following the concentration-driven SS-NEMD simulation procedure described by Ozcan et al.,[62] which allows preserving the concentration gradient of ions between the feed and permeate sides of the COF membrane. Briefly, this approach consists of introducing two separate control regions: an inlet control region (ICR) in the feed side of the COF membrane and an outlet control region (OCR) in the permeate side of the COF membrane, see Figure 2 for a schematic representation. Two transient regions, the inlet transient region (ITR) on the feed side and the outlet transient region (OTR) on the permeate side, separate the COF membrane from the respective control regions. Two separate external forces are applied on the ions localized in two regions: the inlet force region (IFR) located on the feed side adjacent to ICR and the outlet force region (OFR) located on the permeate side adjacent to OCR, so as to regulate the

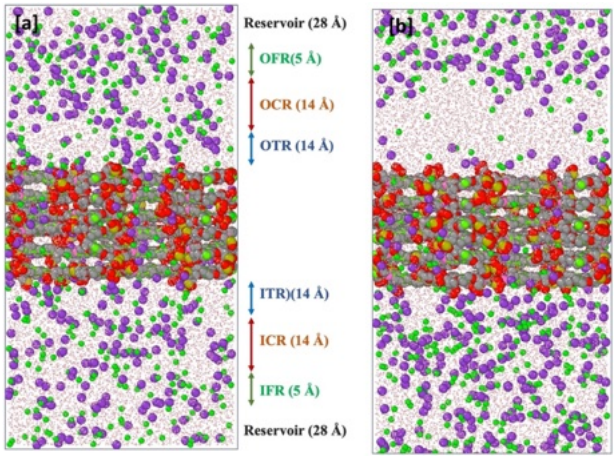

Figure 2. Conceptual representation of the concentration gradient-driven NEMD approach employed in this work. IFR, ICR, and ITR correspond to the inlet-force, inlet-control, and inlet-transient regions, respectively, whereas OTR, OCR, and OFR represent the outlet-transient, outlet-control, and outlet-force regions, respectively. Boundaries of the regions along the "*z*" coordinate of the simulation box are indicated adjacent to the specific regions (in Å). (a) Left and (b) right images correspond to the snapshots of the neutral COF1 (COF1−0q) system in its initial state (before the onset of the SS-NEMD simulation) and after 60 ns of simulation time under the SS-NEMD approach.

https://doi.org/10.1021/acs.jpcb.6c01511
J. Phys. Chem. B 2026, 130, 5775−5790

concentration of ions in the respective control regions. These external forces are perpendicular to the COF membranes and regulate the flux of ions across the IFR/OFR such that the concentration of ions in the ICR/OCR is restrained to a selected target value. By modulating the IFR/OFR forces, two different concentrations in the inlet (ICR) and outlet (OCR) control regions can be imposed by defining these external forces as,

$$F_i^I = k_i^I(n_i^{T,I} - n_i^{\mathrm{ICR}})G^I(z - Z_F^I, \sigma)$$

$$F_i^O = k_i^O(n_i^{T,O} - n_i^{\mathrm{OCR}})G^O(z - Z_F^O, \sigma) \quad (1)$$

where superscripts I and O refer to inlet and outlet, respectively, "i" indicates the ion species subjected to force F, k_i^I and k_i^O are the IFR and OFR force constants, respectively, $n_i^{T,I}$ and $n_i^{T,O}$ are the target concentrations on the feed and permeate sides of the COF membrane, respectively. G^{I} and G^{O} are two bell-shaped functions with width σ centered around Z_F^I and Z_F^O, respectively, serving to localize the application of bias force on the ions within the IFR and OFR, respectively. n_i^{ICR} and n_i^{OCR} are the instantaneous concentrations in the ICR and OCR, calculated as

$$n_i^{\mathrm{CR}} = \frac{1}{V_{\mathrm{CR}}} \sum_j^{N_i} \theta(z_j) \quad (2)$$

where V_{CR} is the volume of the control region, N_i is the total number of ions of a given species "i" in the simulation box, and $\theta(z_j)$ is a selection step function set to 1 if z_j, the coordinate of the selected ion, is inside the given control region (CR) and set to 0 otherwise. The direction (sign) of force F_i changes in such a way that if the number of ions in V_{CR} is higher than the target value, then the force repels the ions toward the bulk (defined as the reservoir); conversely, if the number of ions in V_{CR} is smaller, then the force F_i attracts the ions from the reservoir to the control region. As periodic boundary conditions along the "z" direction are maintained, a steady-state concentration gradient of ions in the ICR and OCR regions is maintained as the ions permeate through the membrane, cross the OCR, and flow back into the ICR through the reservoir, thus establishing a stationary flow of ions.

The permeation of ions through three functionalized COF systems (COF1, COF2, and COF3 as described in Figure 1) was modeled as a function of the degree of negative charges present in the COF pores. More specifically, the SO_3H unit of the functionalized COFs is modulated to contain: (i) 0 negative charges per COF pore, thus containing only SO_3H units; (ii) 3 negative charges per COF pore, with alternating SO_3^- and SO_3H units; and (iii) 6 negative charges per COF pore, thus 6 SO_3^- units. K^+ counterions are used to passivate the negative charges. Unless otherwise specified, the ICR and OCR target concentrations were set to 0.30/0.15 and 0 ions per nm^3, respectively, while the IFR and OFR forces were set to 100 kJ/mol and 1000 kJ/mol, respectively. The target concentration of 0 ions per nm^3 in the OCR was selected to create a vacuum effect on the ions in the permeate side of the COF membranes, which is achieved by setting a larger OFR force constant, k_i^O (≈10 times) compared to that of the IFR force, k_i^I. No forces were set on the water molecules, entailing that the water molecules are diffusing either randomly or under the influence of electro- osmotic water drag associated with the charged ions traversing the COF pores. Ion flux due to the concentration gradient in the z direction, J_z, was calculated by counting the number of ions passing through a cross-sectional plane of area "A_{xy}" positioned at the center of the COF membrane, normalized by the simulation time (t) in the SS-NEMD production run, given by

$$J_z = \frac{N_i^+ - N_i^-}{tA_{xy}} \quad (3)$$

where N_i^+ and N_i^- are the number of ions of species "i" passing through the plane of area "A_{xy}" (considered here as the area of the simulation box) in the positive (toward the permeate region) and negative directions (toward the feed region), respectively. The ion transference number (Tr[88,89]) of the (charged) functionalized COFs is then calculated as,

$$\mathrm{Tr}_q = \frac{J_z^{\mathrm{K^+/Cl^-}}}{J_z^{\mathrm{K^+}} + J_z^{\mathrm{Cl^-}}} \quad (4)$$

where q = 0, −3, or −6 represents the charge in the nanoporous domains of the COF membrane, $J_z^{\mathrm{K^+}}$ and $J_z^{\mathrm{Cl^-}}$ represent the ion flux of the K^+ and Cl^- ions through the (charged) functionalized COF membranes, respectively. When ion diffusion coefficients are employed instead of ionic fluxes, eq 4) can be applied accordingly.

In the following sections, using the SS-NEMD approach and considering COF1 as a model system, we first discuss the effect of the group density of negative charge per COF1 pore on the resulting K^+ and Cl^- ion flux/diffusivity and transference number values, considered (i) as a function of the total molar concentration of ions in the simulation cell using concentrations of 0.2 and 0.4 M and (ii) as a function of ICR target ion concentrations of 0.3 per nm^3 (≈0.49 mol/L) and 0.15 per nm^3 (≈0.24 mol/L) under an OCR target ion concentration of 0 ions per nm^3. The ICR target concentration of 0.3 ions/nm^3 (≈0.49 mol/L) is reminiscent of real systems like seawater, where the ion concentration is ∼0.6 mol/L. In contrast, a concentration of 0.15 ions/nm^3 (≈0.24 mol/L) would represent an intermediate case- with a moderately diluted ionic environment that is higher than physiological fluids (∼0.15 mol/L) but lower than seawater. These results are also compared with conventional nonequilibrium "slab-MD" simulations wherein K^+ and Cl^- ions were placed only on the feed side of the COF1 membranes while the permeate side contains no ions, similar to the work of Cao et al.,[54] to provide a quantitative assessment between the two approaches. The choice of using two different ICR target ion concentrations in SS-NEMD simulations is to analyze/understand, if the imposed concentration gradient across the COF membranes modulates ion permselectivity due to a possible variation in concentration polarization at the membrane-solvent interfaces, as typically observed in ion exchange membranes.[90,91] Subsequently, we discuss the effect of functionalization of COF-DT membranes with sulfonic acid-terminated oligo(n)-ethylene glycol; n = 2 and 3 (aka COF2 and COF3, respectively) with respect to COF1 membranes at fixed ICR and OCR target concentrations of 0.30/0.15 and 0 ions per nm^3, respectively, demonstrating that such functionalization can indeed enhance both the positive ion flux and the corresponding ion selectivity and/or ion transference numbers.

https://doi.org/10.1021/acs.jpcb.6c01511
J. Phys. Chem. B 2026, 130, 5775−5790

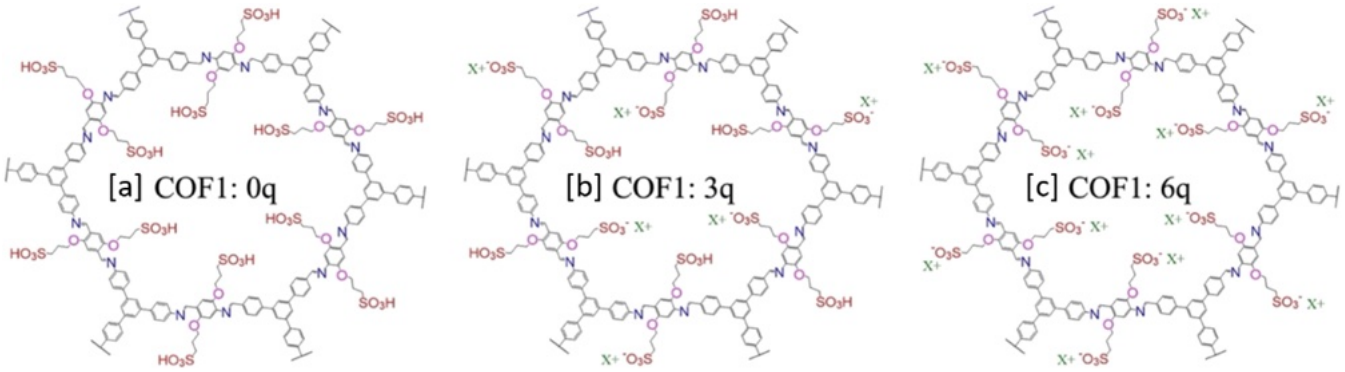

Figure 3. Schematic representation of the COF1 variants with (a) left: 0 negative charges per COF1 pore containing only neutral SO_3H units; (b) middle: 3 negative charges per COF1 pore, containing 3 alternating negatively charged SO_3^- and 3 neutral SO_3H units; and (c) right: 6 negative charges per COF1 pore, containing 6 negatively charged SO_3^- units. X^+ represents the K^+ counterions used to passivate these negative charges.

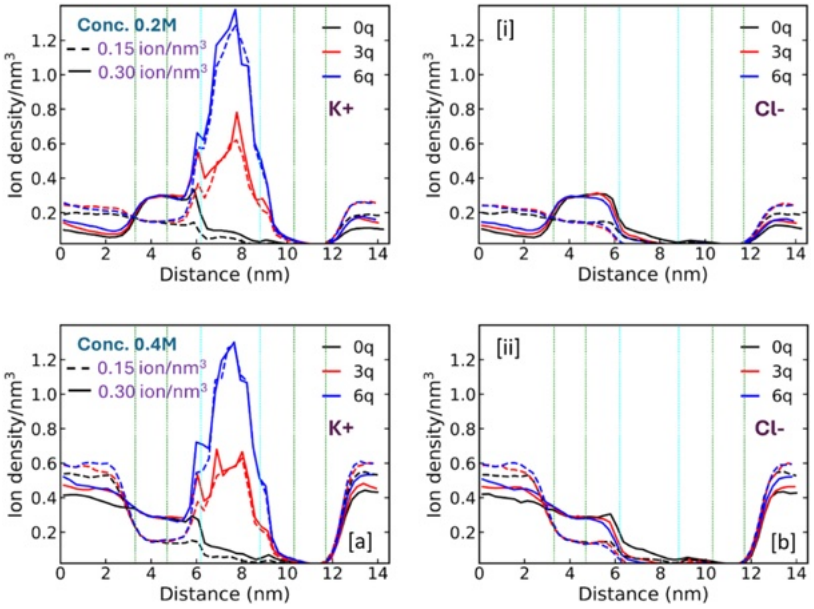

Figure 4. Concentration profiles (1D ion number-density) plots for (a) left: K^+ and (b) right: Cl^- ions, as a function of the SS-NEMD simulation box length along the "z" coordinate (represented by the x-axis of the plots) and averaged over ≈60 ns of SS-NEMD production runs for ICR target ion concentrations of 0.15 per nm^3 (dashed lines) and 0.30 per nm^3 (solid lines) and for molar concentrations of ions in the simulation cell of (i) top: 0.2 M and (ii) bottom: 0.4 M, respectively. The regions between the green dotted lines represent the ICR (centered at ≈4 nm) and OCR (centered at ≈11 nm) regions, respectively. The regions between the dotted cyan lines (centered at ≈7.5 nm) represent the COF membrane.

3. RESULTS AND DISCUSSION

3.1. Ion Permeation through Charged COF1 Membranes

Neutral and negatively charged COF1 membranes were prepared by varying the percentage/group density of negatively charged units per pore. While the SO_3H units of COF1 are left unaltered to represent the 0 negative charge case, hitherto abbreviated as COF1−0q, protons from three alternating SO_3H units were removed to form SO_3^- units to represent the −3 negative charges case, hitherto abbreviated as COF1−3q, and the protons from all six SO_3H units were removed to form SO_3^- units to represent the −6 negative charges case, hitherto abbreviated as COF1−6q, see Figure 3 for a schematic representation of the COF1 membranes and Supporting Information Table S1 for structural information on COF1−0q, COF1−3q, and COF1−6q membranes along with their DDEC06 charges.

The SS-NEMD simulation setup was prepared by positioning the electrolyte (K^+ and Cl^-) ions, together with K^+ counterions and water molecules in simulation cells containing COF1−0q, COF1−3q, and COF1−6q membranes, respectively, following the procedure described in the Computational Methodology section. For COF1−3q and COF1−6q, K^+ counterions were initially positioned in the vicinity of SO_3^- units to compensate for the negative charges, thus acting as counterions to ensure charge neutrality of the MD simulation box, see Figure 3 for details. SS-NEMD simulations were then performed on all the three variants, and the results are analyzed in terms of the ion density plots, radial distribution functions, and the ion flux/transference numbers.

One-dimensional ion density plots for both K^+ and Cl^- ions, as a function of NEMD simulation box length along the z-coordinate and averaged over ≈60 ns of production runs, are reported in Figure 4. It can be noticed that the target concentration in ICR reaches the predefined values of 0.15 and 0.3 ions per nm^3 while that in the OCR remains very close to the predefined value of 0 ions per nm^3, for both K^+ and Cl^- ions, as denoted by the dashed and solid lines in Figure 4,

https://doi.org/10.1021/acs.jpcb.6c01511
J. Phys. Chem. B 2026, 130, 5775−5790

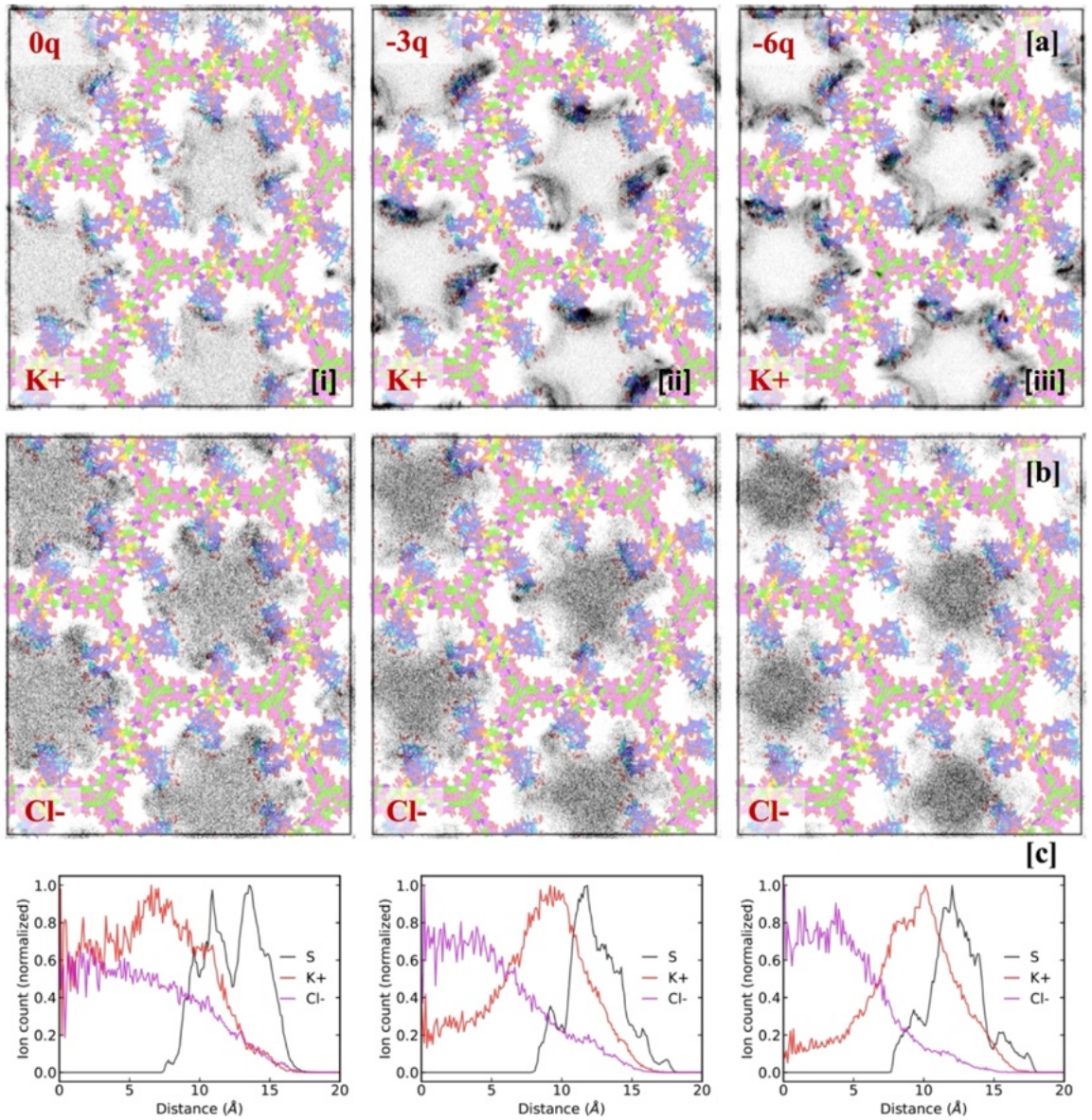

Figure 5. Two-dimensional density maps of (a) top: K^+ and (b) middle: Cl^- ions, along with their (c) relative densities plotted as a function of radial distance from the center of each COF pore, averaged over ≈60 ns of SS-NEMD production runs performed for ICR target densities of 0.3 ions/nm^3 with (i) left: 0 negative charges per COF1 pore containing only neutral SO_3H units; (ii) middle: 3 negative charges per COF1 pore, containing 3 alternating negatively charged SO_3^- and neutral SO_3H units; and (iii) right: 6 negative charges per COF pore, containing 6 negatively charged SO_3^- units. Bottom images (c) represent the normalized relative density of K^+ and Cl^- ions present in the vicinity of -SO_3H groups of COF1 membranes, calculated as a function of radial distance from the center of each COF pore; 0 of the *x*-axis, represented in Å, therefore corresponds to the center of COF1 pore, averaged over ≈60 ns of MD production runs with (i) left: COF1−0q layers, (ii) middle: COF1−3q layers, and (iii) right: COF1−6q layers.

respectively. While the ion densities are higher at the entrance of the membranes, the ion densities through the membrane decrease gradually along the *z*-coordinate of the COF membrane finally edging toward the OCR target of zero concentration. This variation in the number densities along the *z*-coordinate of the SS-NEMD simulation box ensures that the working principle of the concentration gradient approach is properly employed, similar to that reported by Ozcan et al.[62] However, variations in the K^+ and Cl^- ion number densities were observed inside the nanopore when the charge of COF1 membranes was considered. Increasing the percentage of negative charges (COF1−3q and COF1−6q) results in a higher number of K^+ ions within the COF1 nanopores reaching values around 0.15 (0.10), 0.68 (0.60), and 1.34 (1.21) K^+ ions per nm^3 at the center of COF1−0q, COF1−3q, and COF1−6q membranes for predefined ICR target values of 0.3 (0.15) ions per nm^3, respectively, whereas a substantial decrease in the number of Cl^- ions was observed. For predefined ICR target values of 0.3 (0.15) ions per nm^3, the number of K^+ ions in the ITR region also increased with the increase in the percentage of negative units, reaching values around 0.29 (0.18), 0.59 (0.39), and 0.66 (0.60) K^+ ions per nm^3 at the membrane-solvent interface, respectively. This shows that the negative potential imposed by the COF1 membranes on the electrolyte ions not only increases (decreases) the number of K^+ (Cl^-) ions within the COF

https://doi.org/10.1021/acs.jpcb.6c01511
J. Phys. Chem. B 2026, 130, 5775−5790

nanopores but also drags (repels) the K^+ (Cl^-) ions toward and through (away from) the COF1 membranes. The number of K^+ ions in the OTR region also increases with membrane charge, showing that a greater number of K^+ ions are leaving the COF1 membrane.

The pronounced ion density peaks near the membrane-solvent interface and within the membrane region reflect the combined influence of the Donnan exclusion effect and concentration polarization, which is clearly captured by SS-NEMD molecular dynamics simulations under an imposed steady-state concentration gradient. The Donnan effect, originating from fixed negative charges inside the COF1 membrane, strongly attracts K^+ ions while excluding Cl^- ions, resulting in significant enrichment of K^+ ions within the membrane pores (at approximately 6−9 nm positions, as shown in Figure 4). This behavior becomes more evident for COF1 membranes with higher charge states (e.g., COF1−6q), where sharp increases in K^+ ion densities are observed. In parallel, concentration polarization develops in the inlet transition region (ITR, approximately 3−5 nm as shown in Figure 4), where ion accumulation occurs due to the imbalance between convective transport toward the membrane and diffusion back into the bulk solution. At higher imposed concentration gradients (of 0.3 ions/nm^3 in the ICR; solid lines in Figure 4), the driving force for ion migration intensifies, amplifying K^+ accumulation at the inlet interface and increasing the number of K^+ ions within the membrane pores, leading to more pronounced density peaks. The OCR (approximately 10−12 nm, as shown in Figure 4) is maintained at zero ion concentration for both ICR target values of 0.3 and 0.15 ions/nm^3, further reinforcing the directional flux and enhancing K^+ accumulation at the inlet. Collectively, these conditions produce steep ion density gradients across the membrane, with peak magnitudes scaling with both membrane charge and the applied concentration gradient. Interestingly, the total molar concentration of ions in the simulation cell (viz concentrations of 0.2 M and 0.4 M) has very little to no influence on the ion densities in the ITR/OTR and COF regions, entailing that the variation in ion density at the membrane-solvent interface (ITR/OTR regions) and within the COF pores is purely driven by imposed steady-state concentration gradients (0.15 and 0.3 ions/nm^3) between the feed and permeate sides of the membrane. Also, the number of K^+ and Cl^- ions in the ITR/OTR regions and in the COF pores remains constant throughout the SS-NEMD simulations, as a function of simulation time. In contrast, comparing these ion density profiles (obtained using the SS-NEMD approach) to those obtained from conventional nonequilibrium "slab-MD" simulations,[54] we conclude that the concentrations of ions in the feed and permeate sides of the membrane vary with time, implying that a steady-state concentration gradient cannot be established using this "conventional" nonequilibrium MD approach, see Section S2 for details. Therefore, we believe that the concentration gradient-driven ion fluxes/diffusivities and corresponding transference numbers extracted from conventional nonequilibrium approach simulations should be considered with caution.

The 2D density maps (calculated as a function of the z-coordinate by setting the z-coordinate limits to that of the slab thickness) as a function of increasing negative charge of COF1 membranes for ICR target values of 0.30 ions/nm^3 are reported in Figure 5; those computed for ICR target values of 0.15 ions/nm^3 are reported in Figure S6 and follow a similar pattern to that of the 1D density plots reported in Figure 4. Irrespective of the concentration gradients (0.15 and 0.3 ions/nm^3) between the feed and permeate sides of the membrane, in charged COFs, the K^+ ions are highly localized around the -SO_3H units while the Cl^- ions remain spatially confined in the central region of the pores. This effect is exemplified in the radial plot of the relative density of K^+ and Cl^- ions in Figure 5(c). We observe that the K^+ ions move closer to the SO_3^- units while the Cl^- ions get increasingly confined toward the center of the COF1 pore when the percentile in negative charge increases.

The radial density distribution profiles, $g(r)$, give a sharper picture of the ionic distributions inside the pores, see Supporting Information Figure S10. The $g(r)$ computed for K^+ ions and COF1 show sharp peaks between 2 Å and 7 Å, with their intensities increasing with the increase in negative charge percentage. On the other hand, the $g(r)$ computed for Cl^- ions and COF1 are rather structureless, indicating the lack of any specific interaction between these two units. Although $g(r)$ computed for Cl^- ions and that of "S" atom of -SO_3H units shows some structure, its $g(r)$ is very small (∼1.5) when compared to that of K^+ ions and the "S" atom of -SO_3H units (∼20). The observation of such a complex structure for K^+ ions suggests a strong electrostatic interaction between the positively charged K^+ ions and the negatively charged SO_3^- units. Indeed, as reported in Figure S11, the pair interaction energies of K^+ (Cl^-) ions with -SO_3H units of the COF1 membranes increase (decrease) with an increase in negative charge, from around −7 kcal/mol for COF1−0q, to −28 kcal/mol for COF1−3q, and to −36 kcal/mol for COF1−6q membranes. These values are almost identical to the pair interaction energies of K^+ ions with the overall COF1 membranes (including all atoms/units of the membranes) entailing that the interaction is primarily between the K^+ ions and the -SO_3H units of these membranes.

Finally, we computed the ion flux and ion transference numbers (Tr) of K^+ and Cl^- ions as a function of the increasing number of negative charges in the nanopores for steady-state concentration gradients (ICR target values) of 0.15 and 0.3 ions/nm^3 between the feed and permeate sides of the membrane and for total molar concentrations of ions in the simulation cell of 0.2 M and 0.4 M. As reported in Figure 6, the flux of K^+ ions increases with the percentage increase of negative charges, whereas that of Cl^- ions decreases, irrespective of the total molar concentration of ions in the SS-NEMD simulation cell. However, the absolute values of K^+ and Cl^- ion fluxes depend on the imposed/predefined concentration gradients (ICR target values) of 0.15 and 0.3 ions/nm^3. More specifically, the flux of K^+ and Cl^- ions in COF1−0q membranes is almost identical and around 2.3 nm^{-2} ps^{-1} and 1.3 nm^{-2} ps^{-1} for ICR target densities of 0.15 and 0.3 ions/nm^3 respectively, meaning that the functionalized COF1 membranes with no net negative charge in the nanopores do not show any ion selectivity. As the density of negative charges is increased to −3q and −6q, the flux of K^+ ions increases substantially, reaching values of around 4.6 (2.9) nm^{-2} ps^{-1} and 6.1 (4.5) nm^{-2} ps^{-1} for COF1−3q and COF1−6q membranes, respectively, when the ICR target densities are set to 0.30 (0.15) ions/nm^3. On the contrary, the flux of Cl^- ions drastically decreases with an increase in the percentage of negative charges, down to values of around 1.3 (0.6) nm^{-2} ps^{-1} and 0.8 (0.1) nm^{-2} ps^{-1} for COF1−3q and for COF1−6q

https://doi.org/10.1021/acs.jpcb.6c01511
J. Phys. Chem. B 2026, 130, 5775−5790

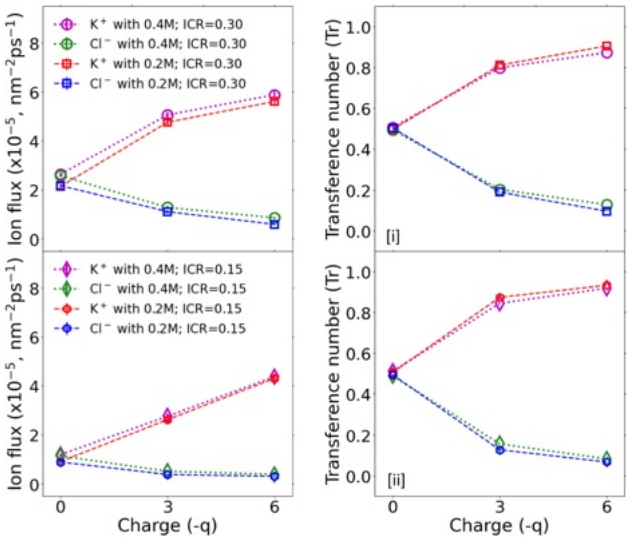

Figure 6. Variation of K^+ and Cl^- ion fluxes (left) and corresponding transference numbers (right) as a function of negative charges within the nanoporous domains of COF1 membranes, extracted from over ≈60 ns of SS-NEMD simulations for ICR target ion concentrations (or concentration gradients between feed and permeate sides) of (i) top: 0.30 per nm^3 (circles and squares) and (ii) bottom: 0.15 per nm^3 (diamonds and hexagons), with the total molar concentration of ions in the simulation cell set to 0.2 M and 0.4 M. Lines are guides to the eye.

membranes, respectively, when the ICR target densities are set to 0.30 (0.15) ions/nm^3. In line with the increase (decrease) of K^+ (Cl^-) ion flux, as a function of the increase in negative charge of COF1 membranes, the ion transference numbers for K^+ ions also increase with increasing negative charges and are significantly larger for K^+ ions than for Cl^- ions (reaching values of around 0.81 for K^+ ions and 0.21 for Cl^- ions in COF1−3q membranes and around 0.90 for K^+ ions and 0.15 for Cl^- ions in COF1−6q membranes, respectively), see Figure 6 (right images), irrespective of the imposed/predefined concentration gradients (ICR target values) of 0.15 and 0.3 ions/nm^3. However, the transference numbers are slightly higher, especially for COF1−3q membranes, for simulations performed at ICR target values of 0.15 ions/nm^3, which could be attributed to reduced concentration polarization at lower concentration gradients as seen from Figure 4. Similar trends were also observed when the ion diffusion coefficients and the corresponding transference numbers were extracted, see Figure S12 for details. This suggests that a mere functionalization of the COF-DT membranes to contain propanesulfonic acid is not enough to ensure selective permeation of K^+ vs Cl^- ions and that the presence of negatively charged SO_3^- groups within the COF1 nanopores is vital to ensure ion selectivity, emphasizing the need for controlled/selective deprotonation of SO_3H units to generate SO_3^- sites under variable experimental conditions.

Furthermore, combining the faster permeation (ion fluxes and MSDs) of cations through negatively charged COF1 membranes together with the analysis of MD trajectories and the 2D density plots, as reported in Figure 5 (where the K^+ ions traverse closer to the SO_3^- units while the Cl^- ions are confined toward the center of the COF pore), it can be inferred that the transport/permeation mechanism of positive (K^+) ions in charged/functional COF membranes follows a "Grotthuss-like" mechanism around the charged -SO_3H units while that of the negative (Cl^-) ions involves a "vehicular" transport, traversing around the center of COF pores.

3.2. Ion Permeation through Functionalized Charged COF Membranes: On the Effect of Glycolated Chains

Having assessed the transport of ions in COF1 membranes with COF pores decorated by propane-sulfonic acid groups, we now focus on the role of the oligo(n)-ethylene glycol linkers; n = 2 and 3, aka COF2 and COF3, respectively, in modulating the ion flux and ion transference numbers. To this end, we compare the results of COF2 and COF3 membranes with respect to those obtained for COF1 (analyzed in terms of the ion density plots, radial distribution functions, and the ion flux/transference numbers extracted from the SS-NEMD simulations performed for imposed/predefined steady-state concentration gradients (ICR target values) of 0.15 and 0.3 ions/nm^3). For simulations with COF2 and COF3 membranes, the total molar concentration of ions was set at 0.4 M, as no significant difference was observed between the simulation results obtained with 0.4 and 0.2 M simulations performed on COF1 membranes, as reported in the previous section.

From the 1D ion density plots of COF2 and COF3 membranes, as reported in Figure 7, it can be noticed that the target concentration in ICR reaches the predefined values of 0.15 and 0.3 ions per nm^3 while that in the OCR remains very close to the predefined value of 0 ions per nm^3, for both K^+ and Cl^- ions, similar to what was observed for COF1 membranes (see Figure 4 for reference). Also, the 1D profile of K^+ and Cl^- ions in COF2 membranes resembles that of COF1 membranes to a large extent (see Figure 4 for comparison). Only a small decrease in the ion density of K^+ ions within the COF2 membranes (1.2 ions/nm^3 as against 1.34 ions/nm^3 for −6q charge in COF1) and a small increase in the ion density of K^+ ions within the ITR regions of COF2 membranes (0.72 ions/nm^3 as against 0.66 ions/nm^3 for −6q charge in COF1) could be observed; both of which could be attributed to the decrease in pore size/volume of COF2 when compared to COF1 and the presence of glycolated chains in COF2 electrostatically attracting K^+ ions, respectively. However, significant changes could be observed when the 1D profiles of K^+ ions in COF3 membranes are compared to that of COF1 membranes.

More specifically, the density of K^+ ions within the COF3 membranes reaches only a value of around 1.0 ions/nm^3 (against 1.34 ions/nm^3 for −6q charge in COF1), which could be attributed to the decrease in pore size of COF3 (due to the oligo(3)-ethylene glycol linkers) when compared to that of COF1. But a significant increase in the ion density of K^+ ions within the ITR regions of COF3 membranes was observed (0.9 ions/nm^3 against 0.66 ions/nm^3 for −6q charge in COF1), meaning that the combined influence of the Donnan exclusion effect and concentration polarization becomes dominant in these membranes. Indeed, the pair interaction energies of K^+ ions with -SO_3H units of the COF3 membranes remain similar to that of COF1 membranes, with values of approximately −8 kcal/mol for COF3−0q, to −29 kcal/mol for COF3−3q, and to −35 kcal/mol for COF3−6q membranes, against −7 kcal/mol for COF1−0q, to −28 kcal/mol for COF1−3q, and to −36 kcal/mol for COF1−6q membranes. But the pair interaction energies of K^+ ions with the overall COF3 membranes (including all atoms/units of the

https://doi.org/10.1021/acs.jpcb.6c01511
J. Phys. Chem. B 2026, 130, 5775−5790

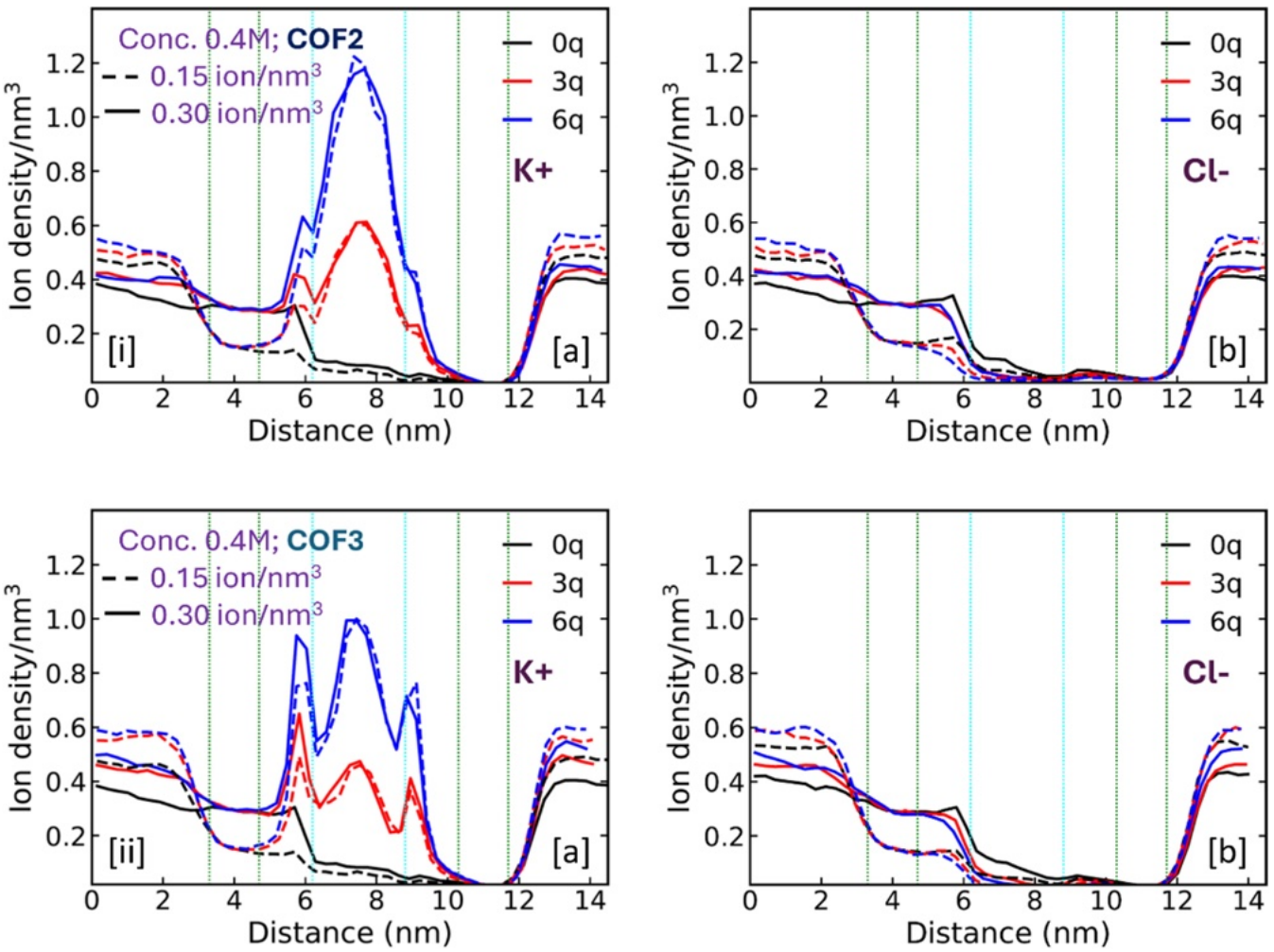

Figure 7. Concentration profiles (1D ion number-density) plots of (i) top: COF2 and (ii) bottom: COF3 for (a) left: K^+ and (b) right: Cl^- ions, as a function of the SS-NEMD simulation box length along the "*z*" coordinate (represented by the *x*-axis of the plots) and averaged over ≈60 ns of SS-NEMD production runs for ICR target ion concentrations of 0.15 per nm^3 (dashed lines) and 0.30 per nm^3 (solid lines) under the total molar concentration of ions in the simulation cell of 0.4 M. The regions between the green dotted lines represent the ICR (centered at ≈4 nm) and OCR (centered at ≈11 nm) regions, respectively. The regions between the dotted cyan lines (centered at ≈7.5 nm) represent the COF membrane.

Table 1. Average Pair Interaction Energies, in kcal/mol, of K^+ and Cl^- Ions with Only the -SO_3H Units of the COF Membranes (Referred to as $COF_{SO3(H)}$ in the Table) and with the Overall COF Membranes Including All the Atoms/Units of Constituting the Membranes (Referred to as COF_{Total} in the Table), Normalized, Respectively, with the Total Number of K +/Cl^- Ions Present in the Vicinity of the COF Membranes (i.e., Thickness of the Membrane with a Tolerance of 5 Å, to Include Boundary Effects, if Any)

	COF1		COF2		COF3	
Ion/COF type and COF Charge	$COF_{SO3(H)}$	COF_{Total}	$COF_{SO3(H)}$	COF_{Total}	$COF_{SO3(H)}$	COF_{Total}
K+; COF−0q	−7 ± 1	−5 ± 1	−8 ± 1	−12 ± 1	−8 ± 1	−16 ± 1
K+; COF−3q	−28 ± 2	−25 ± 2	−29 ± 2	−35 ± 2	−29 ± 2	−38 ± 2
K+; COF−6q	−36 ± 2	−33 ± 2	−35 ± 2	−42 ±2	−36 ± 2	−49 ± 2
Cl^-; COF−0q	+0.32	−0.90	+0.35	+1.66	+0.35	+1.46
Cl^-; COF−3q	+0.26	+0.02	+0.36	+2.41	+0.33	+2.01
Cl^-; COF−6q	+0.32	+0.15	+0.34	+2.96	+0.34	+2.92

membranes) increased to around −16 kcal/mol for COF3−0q, to −38 kcal/mol for COF3−3q, and to −49 kcal/mol for COF3−6q membranes, respectively, see Table 1 for details. In comparison, the pair interaction energies of K^+ ions with the overall COF2 membranes (including all atoms/units of the membranes) are around −12 kcal/mol for COF2−0q, −35 kcal/mol for COF2−3q, and −42 kcal/mol for COF2−6q membranes. This increase in pair interaction energies between K^+ ions and COF2/COF3 membranes indicates that the oligo-ethylene glycol linkers of COF2 and COF3 membranes impose an additional electrostatic attraction on the positively charged K^+ ions, enhancing the combined influence of the Donnan exclusion effect and concentration polarization effect, as observed by the increase in ion densities at the membrane-

https://doi.org/10.1021/acs.jpcb.6c01511
J. Phys. Chem. B 2026, 130, 5775−5790

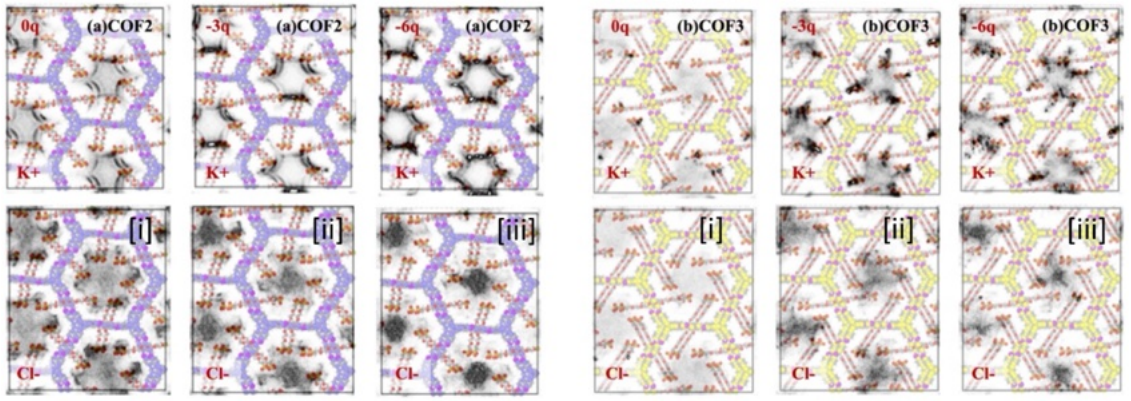

Figure 8. Two-dimensional density maps of (a) COF2 and (b) COF3 membranes averaged over ≈60 ns of NEMD production runs performed using K^+ as counterions passivating the negative charges. Top and bottom images correspond to the density maps of K^+ and Cl^- ions for (i) left: 0 negative charges per COF2/COF3 pore containing only neutral SO_3H units (0q), (ii) middle: 3 negative charges per COF2/COF3 pore, containing 3 alternating negatively charged SO_3^- and neutral SO_3H units (−3q), and (iii) right: 6 negative charges per COF2/COF3 pore, containing 6 negatively charged SO_3^- units (−6q).

solvent interface of the ITR region (Figure 7). However, as the number of atoms increases from COF1 to COF3 and given the relative variations in the total number of K^+ and Cl^- ions in the vicinity of COF membranes—together with variations in the size of COF pores—the interaction energies between the ions and COF_{Total}, as reported in Table 1, are to be taken with caution.

In comparison, the 2D density maps for both K^+ and Cl^- ions in COF2 and COF3 membranes, averaged over 60 ns of production runs, reported in Figure 8, reveal that the K^+ ions are localized around the -SO_3H units, whose concentration increases with the negative charge of COF2/COF3 membranes. By comparison, the Cl^- ions remain spatially confined in the center of the nanopores, a behavior that is reminiscent to what was observed in COF1. Small differences can be reported, however. The K^+ ions are spatially localized within the COF2 pores, concentrated mainly around the -SO_3H units, whereas in COF3 pores, they appear to be partly delocalized. This effect can be attributed to the flexible and mobile nature of 3-ethylene glycol chains in water and also to the additional electrostatic interaction between the glycol chains and the K^+ ions, as reported above. This spatial confinement of Cl^- ions at the center of the pores increases with the increase in negative charges per COF pore and with the increase in the length of ethylene glycol chains, which could be attributed, in part, to the reduction of solvent-accessible area within the COF pores due to extended chain lengths. Careful examination of Figures 7 and 8 also suggests that the K^+ ions (concentrated around the -SO_3H units of the COF membranes) tend to shield the Cl^- ions from the pore edges, which are consequently pushed toward the center of the pore.

Radial density distribution profiles, $g(r)$, between the K^+ ions and COF2/COF3 membranes show peaks that extend between 7 Å and 10 Å in addition to the sharp peaks between 2 Å and 7 Å observed in COF1 membranes, the intensities of which also increase with the increase in negative charges per COF pore, see Supporting Information Figures S13 and S14 for details. This structure further asserts that there is indeed a strong interaction not only between the positively charged K^+ ions and the negatively charged SO_3^- units but also, quite expectedly, between K^+ ions and the oxygen atoms of the glycolated chains. On the contrary, radial density distribution profiles between the Cl^- ions and COF2/COF3 membranes are rather structureless, suggesting the lack of any specific interaction between the two units.

Conclusively, we analyzed the ion flux and ion transference numbers (Tr) of K^+ and Cl^- ions as a function of the percentage of negative charges in the nanopores for the COF2 and COF3 membranes to have a quantitative comparison on the role of sulfonic acid-terminated oligo(n)-ethylene glycol groups in modulating the ion flux and/or ion selectivity with respect to the COF1 membranes. Similar trends were observed for COF1, COF2, and COF3 membranes, i.e., the ion flux of K^+ (Cl^-) ions increases (decreases) with the increase in negative charges, as reported in Figure 9.

However, we observe that while the flux of K^+ ions is only marginally lowered in COF2 and COF3 membranes when compared to that of the COF1 membranes, the flux of Cl^- ions is reduced considerably (by around 50%, see Figure 6 for comparison). Such a decrease of ion flux in COF2 and COF3 membranes can partly be attributed to the reduction of effective pore size in COF2/COF3 membranes, with the effective surface area (solvent-accessible volume) of COF pores decreasing by around 3.8% in COF2 and by around 12.4% in COF3, in comparison to COF1, with respective values of 31.32 nm^2 (80.81 nm^3), 30.31 nm^2 (77.75 nm^3) and 27.45 nm^2 (70.81 nm^3) for COF1, COF2, and COF3 membranes. In addition, the marginal decrease of K^+ ion flux in COF2 and COF3 membranes can also be partly attributed to the (i) spatial confinement of K^+ ions in the nanoporous domains and (ii) a resultant increase in K^+ ion concentration locally, as seen from Figure 8. The decrease of Cl^- ion flux, on the other hand, can also be attributed to the reduced number of Cl^- ions present within the nanoporous domains of COF2 and COF3 membranes when compared to that of the COF1 membrane, endorsed by the presence of oxygen atoms on the glycolated chains that repel the negatively charged ions. Indeed, the number of Cl^- ions present within the COF3−6q (COF2−6q) nanopores decreases substantially by around 57% (34%) when compared to COF1−6q. Altogether, the ion transference numbers of K^+ (Cl^-) ions in COF2/COF3 membranes are higher (lower) when compared to the COF1, meaning that the functionalization of COF-DT membranes with oligo(n)-ethylene glycol chains increases the ion selectivity of the respective membranes despite the decrease in effective surface area and solvent-accessible volume of

https://doi.org/10.1021/acs.jpcb.6c01511
J. Phys. Chem. B 2026, 130, 5775−5790

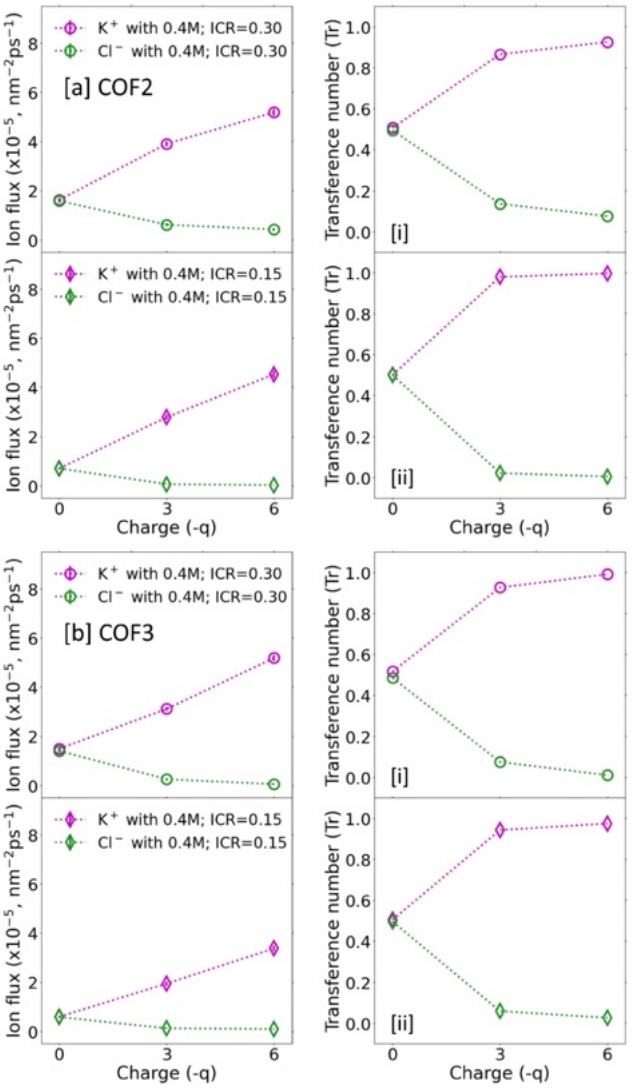

Figure 9. Variation of K^+ (purple) and Cl^- (green) ion fluxes and ion transference numbers in (a) top: COF2 and (b) bottom: COF3 membranes as a function of negative charges within the nanoporous domains, extracted from over ≈60 ns of SS-NEMD production runs for ICR target ion concentrations (or concentration gradients between feed and permeate sides) of (i) top: 0.30 per nm^3 (circles) and (ii) bottom: 0.15 per nm^3 (diamonds), with the total molar concentration of ions in the simulation cell set to 0.4 M. Lines are guides to the eye.

COF2 and COF3 pores. More specifically, for a concentration gradient of 0.3 ions/nm^3 (ICR target value), the ion transference numbers of K^+ ions increase while that of Cl^- ions decrease with the increase in the number of negative charges of COF2 and COF3 membranes with corresponding values of 0.95 and 0.10 in COF2−6q membranes and 0.99 and 0.06 in COF3−6q, respectively (higher than the 0.90 and 0.15 values for K^+ and Cl^- ions obtained in the COF1−6q membrane). When the concentration gradient is reduced from 0.3 ions/nm^3 to 0.15 ions/nm^3 (ICR target value), these values for K^+ (Cl^-) ions become even larger (smaller), reaching approximately 0.99 (0.1) and 0.99 (0.04) for COF2−6q and COF3−6q membranes, respectively, against 0.92 and 0.10 values for K^+ and Cl^- ions obtained in the COF1−6q membrane. Similar trends were also observed when the ion diffusion coefficients and the corresponding transference numbers were extracted, see Figures S15 and S16 for details. This increase in transference number and therefore the increase in ion permselectivity at reduced concentration gradients (smaller ICR target values) can be attributed to reduced concentration polarization at the membrane-solvent interface in the ITR region, as can clearly be seen from Figure 7, enabling faster permeation of ions through the membrane. Interestingly, the transference numbers of COF2 and COF3 are very similar for COF−3q (partially charged) and COF−6q membranes (fully charged), reaching around 99% efficiency in cation selectivity even for partially charged systems (COF2−3q and COF3−3q) which was not the case for COF1 membranes, where the efficiency reaches only around 80% for COF1−3q and around 90% for COF1−6q.

Therefore, functionalizing COF-DT membranes to contain oligo(n)-ethylene glycol chains not only facilitates a way to tune the effective pore size of COF membranes but also provides a way to improve/modulate their ion selectivity ratios when compared to the alkyl functionalization. However, as exemplified in the previous sections, a mere functionalization of the COF membranes to contain either propanesulfonic acid or sulfonic acid-terminated oligo(n)-ethylene glycols is not enough to ensure K^+ over Cl^- ion permselectivity, as all the neutral COF−0q variants studied in this work show no specific ion selectivity. Only the presence of negatively charged SO_3^- groups within the COF-DT nanopores, attained possibly via the tuning of SO_3H deprotonation under variable/selective experimental conditions, can ensure cation selectivity, thus enabling the negatively charged COFs as ion permselective membranes and as active membranes for osmotic energy harvesting.

4. CONCLUSIONS

Ion permeation in functionalized and negatively charged COF membranes decorated to contain either propanesulfonic acid or sulfonic acid-terminated oligo(n)-ethylene glycol chains, n = 2 and 3, was studied as a function of the degree of (percentage of) negatively charged groups decorating the COF membranes. State-of-the-art "steady-state" nonequilibrium molecular dynamics (SS-NEMD) simulations were employed to accurately and realistically model the concentration-driven ion permeation process in a finite array of COF layers, and the results were analyzed in terms of ion diffusivity, ion flux, and ion transference numbers. We demonstrate that the cation (anion) permeation in a finite array of COF membranes increases (decreases) with the degree of charged groups decorating the COF membranes. We further show that the COF membranes decorated with charged oligo(n)-ethylene glycol chains lead to enhanced ion selectivity ratios compared to the COF membranes with alkylated chains, reaching ion permselectivity efficiencies of around 99%. Remarkably, this enhancement occurs despite a noticeable decrease in the effective surface area of COF nanoporous domains, endorsed by the glycol-oxygen atoms that attract (repel) and drive the cations (anions) through (away-from) the COF membranes. Functionalizing COF-DT membranes to contain oligo(n)-ethylene glycol chains terminated with acidic functional groups such as sulfonic acid, phosphonic acid, or carboxylic acid can thus provide a unique way to not only modulate the effective pore size of the COF membranes but also to tune the degree of charged groups (charge density) in COF nanoporous domains, both of which can further enhance the ion selectivity ratios of resultant COF variants to be used as ion permselective

https://doi.org/10.1021/acs.jpcb.6c01511
J. Phys. Chem. B 2026, 130, 5775−5790

membranes and/or in osmotic/blue energy generators. Although only relatively thin (six-layer) COF membranes were considered in this work due to computational constraints, we anticipate that increasing the membrane thickness would further modulate K^+ and Cl^- ion diffusion through enhanced confinement effects and transport resistance, potentially altering ionic permeability and selectivity. This aspect warrants systematic investigation in future studies, particularly in the context of commercially relevant ion-exchange membranes such as Nafion and Sustainion, which typically exhibit thicknesses on the order of 150−300 μm.

■ ASSOCIATED CONTENT

Supporting Information

The Supporting Information is available free of charge at https://pubs.acs.org/doi/10.1021/acs.jpcb.6c01511.

Details on DFT potential energy surface calculations of different COF stacking modes, including computational parameters and energetic analysis; structural models and schematic representations of pristine and functionalized COFs; simulated diffraction patterns for various stacking configurations; atomic coordinates, unit cell parameters, and DDEC6-derived partial charges for COF systems with varying charge states; detailed molecular dynamics simulation protocols, including a comparison of conventional nonequilibrium "slab-MD" simulations and steady-state nonequilibrium MD approaches; analysis of ion transport behavior through COF membranes, including time evolution of ion populations, spatial ion distributions, and density maps; radial distribution functions describing ion-membrane interactions; ion-COF interaction energies; calculations of mean square displacements, diffusion coefficients, and transference numbers; and visualization of ion transport dynamics from molecular dynamics trajectories (PDF)

■ AUTHOR INFORMATION

Corresponding Authors

Pascal Damman − *Interfaces and Complex Fluids Laboratory, University of Mons, Mons 7000, Belgium*; Email: pascal.damman@umons.ac.be

David Beljonne − *Laboratory for Chemistry of Novel Materials, University of Mons, Mons 7000, Belgium*; orcid.org/0000-0002-2989-3557; Email: david.beljonne@umons.ac.be

Authors

Sai Manoj Gali − *Laboratory for Chemistry of Novel Materials, University of Mons, Mons 7000, Belgium; Flemish Institute for Technology and Research (VITO), Mol 2400, Belgium*; orcid.org/0000-0002-0388-7888

Quentin Thomas − *Laboratory for Chemistry of Novel Materials, University of Mons, Mons 7000, Belgium; Interfaces and Complex Fluids Laboratory, University of Mons, Mons 7000, Belgium*

Nicolas Karageorgos − *Laboratory for Chemistry of Novel Materials, University of Mons, Mons 7000, Belgium*; orcid.org/0009-0008-5080-9058

Nicolas Rolland − *Laboratory for Chemistry of Novel Materials, University of Mons, Mons 7000, Belgium; Univ. Lille, CNRS, Centrale Lille, Univ. Artois, UMR 8181 − UCCS − Unité de Catalyse et Chimie du Solide, Lille F-59000, France*

Complete contact information is available at: https://pubs.acs.org/10.1021/acs.jpcb.6c01511

Author Contributions

S.M.G. performed the periodic DFT calculations and prepared the systems for MD simulations. S.M.G., Q.T., and N.K. performed the SS-NEMD and slab-MD simulations, with S.M.G. and Q.T. contributing equally. N.R., P.D., and D.B. supervised the work. P.D. and D.B. conceived and designed the study. All authors discussed the results and contributed to the interpretation of the data as well as to the writing and editing of the manuscript. S.M.G. and Q.T. contributed equally to this work.

Author Contributions

#Sai Manoj Gali and Quentin Thomas contributed equally to this work.

Notes

The authors declare no competing financial interest.

■ ACKNOWLEDGMENTS

This work was supported by the Belgian National Fund for Scientific Research (FRS-FNRS) within the Consortium des Équipements de Calcul Intensif − CÉCI, under Grant 2.5020.11, and by the Walloon Region (ZENOBE Tier-1 supercomputer, under grant no. 1117545, and LUCIA Tier-1 supercomputer under grant no. 1910247). S.M.G. was Chargé de Recherche (FNRS), and P.D. and D.B. are FNRS Research Directors.

■ REFERENCES

(1) Liu, K.; Qi, H.; Dong, R.; Shivhare, R.; Addicoat, M.; Zhang, T.; Sahabudeen, H.; Heine, T.; Mannsfeld, S.; Kaiser, U.; Zheng, Z.; Feng, X. On-Water Surface Synthesis of Crystalline, Few-Layer Two-Dimensional Polymers Assisted by Surfactant Monolayers. *Nat. Chem.* **2019**, *11* (11), 994−1000.

(2) Joshi, T.; Chen, C.; Li, H.; Diercks, C. S.; Wang, G.; Waller, P. J.; Li, H.; Bredas, J.; Yaghi, O. M.; Crommie, M. F. Local Electronic Structure of Molecular Heterojunctions in a Single-Layer 2D Covalent Organic Framework. *Adv. Mater.* **2019**, *31* (3), 1805941.

(3) Dogru, M.; Handloser, M.; Auras, F.; Kunz, T.; Medina, D.; Hartschuh, A.; Knochel, P.; Bein, T. A Photoconductive Thienothiophene-Based Covalent Organic Framework Showing Charge Transfer Towards Included Fullerene. *Angew. Chem., Int. Ed.* **2013**, *52* (10), 2920−2924.

(4) Medina, D. D.; Werner, V.; Auras, F.; Tautz, R.; Dogru, M.; Schuster, J.; Linke, S.; Döblinger, M.; Feldmann, J.; Knochel, P.; Bein, T. Oriented Thin Films of a Benzodithiophene Covalent Organic Framework. *ACS Nano* **2014**, *8* (4), 4042−4052.

(5) Côté, A. P.; Benin, A. I.; Ockwig, N. W.; O'Keeffe, M.; Matzger, A. J.; Yaghi, O. M. Porous, Crystalline, Covalent Organic Frameworks. *Science* **2005**, *310* (5751), 1166−1170.

(6) El-Kaderi, H. M.; Hunt, J. R.; Mendoza-Cortés, J. L.; Côté, A. P.; Taylor, R. E.; O'Keeffe, M.; Yaghi, O. M. Designed Synthesis of 3D Covalent Organic Frameworks. *Science* **2007**, *316* (5822), 268−272.

(7) Wan, S.; Guo, J.; Kim, J.; Ihee, H.; Jiang, D. A. Belt-Shaped, Blue Luminescent, and Semiconducting Covalent Organic Framework. *Angew. Chem., Int. Ed.* **2008**, *47* (46), 8826−8830.

(8) Wan, S.; Guo, J.; Kim, J.; Ihee, H.; Jiang, D. A Photoconductive Covalent Organic Framework: Self-Condensed Arene Cubes Composed of Eclipsed 2D Polypyrene Sheets for Photocurrent Generation. *Angew. Chem., Int. Ed.* **2009**, *48* (30), 5439−5442.

(9) Ding, X.; Feng, X.; Saeki, A.; Seki, S.; Nagai, A.; Jiang, D. Conducting Metallophthalocyanine 2D Covalent Organic Frameworks: The Role of Central Metals in Controlling π-Electronic Functions. *Chem. Commun.* **2012**, *48* (71), 8952.
(10) Ding, X.; Guo, J.; Feng, X.; Honsho, Y.; Guo, J.; Seki, S.; Maitarad, P.; Saeki, A.; Nagase, S.; Jiang, D. Synthesis of Metallophthalocyanine Covalent Organic Frameworks That Exhibit High Carrier Mobility and Photoconductivity. *Angew. Chem., Int. Ed.* **2011**, *50* (6), 1289−1293.
(11) Jin, E.; Asada, M.; Xu, Q.; Dalapati, S.; Addicoat, M. A.; Brady, M. A.; Xu, H.; Nakamura, T.; Heine, T.; Chen, Q.; Jiang, D. Two-Dimensional Sp 2 Carbon−Conjugated Covalent Organic Frameworks. *Science* **2017**, *357* (6352), 673−676.
(12) Wang, M.; Fu, S.; Petkov, P.; Fu, Y.; Zhang, Z.; Liu, Y.; Ma, J.; Chen, G.; Gali, S. M.; Gao, L.; Lu, Y.; Paasch, S.; Zhong, H.; Steinrück, H.-P.; Cánovas, E.; Brunner, E.; Beljonne, D.; Bonn, M.; Wang, H. I.; Dong, R.; Feng, X. Exceptionally High Charge Mobility in Phthalocyanine-Based Poly(Benzimidazobenzophenanthroline)-Ladder-Type Two-Dimensional Conjugated Polymers. *Nat. Mater.* **2023**, *22* (7), 880−887.
(13) Furukawa, H.; Yaghi, O. M. Storage of Hydrogen, Methane, and Carbon Dioxide in Highly Porous Covalent Organic Frameworks for Clean Energy Applications. *J. Am. Chem. Soc.* **2009**, *131* (25), 8875−8883.
(14) Zeng, Y.; Zou, R.; Zhao, Y. Covalent Organic Frameworks for CO 2 Capture. *Adv. Mater.* **2016**, *28* (15), 2855−2873.
(15) Du, Y.; Yang, H.; Whiteley, J. M.; Wan, S.; Jin, Y.; Lee, S.; Zhang, W. Ionic Covalent Organic Frameworks with Spiroborate Linkage. *Angew. Chem., Int. Ed.* **2016**, *55* (5), 1737−1741.
(16) Royuela, S.; Almarza, J.; Mancheño, M. J.; Pérez-Flores, J. C.; Michel, E. G.; Ramos, M. M.; Zamora, F.; Ocón, P.; Segura, J. L. Synergistic Effect of Covalent Bonding and Physical Encapsulation of Sulfur in the Pores of a Microporous COF to Improve Cycling Performance in Li-S Batteries. *Chem.− Eur. J.* **2019**, *25* (53), 12394−12404.
(17) Li, H.; Pan, Q.; Ma, Y.; Guan, X.; Xue, M.; Fang, Q.; Yan, Y.; Valtchev, V.; Qiu, S. Three-Dimensional Covalent Organic Frameworks with Dual Linkages for Bifunctional Cascade Catalysis. *J. Am. Chem. Soc.* **2016**, *138* (44), 14783−14788.
(18) Koros, W. J.; Zhang, C. Materials for Next-Generation Molecularly Selective Synthetic Membranes. *Nat. Mater.* **2017**, *16* (3), 289−297.
(19) Yuan, S.; Li, X.; Zhu, J.; Zhang, G.; Van Puyvelde, P.; Van der Bruggen, B. Covalent Organic Frameworks for Membrane Separation. *Chem. Soc. Rev.* **2019**, *48* (10), 2665−2681.
(20) Yang, X.; Hu, Y.; Dunlap, N.; Wang, X.; Huang, S.; Su, Z.; Sharma, S.; Jin, Y.; Huang, F.; Wang, X.; Lee, S.; Zhang, W. A Truxenone-based Covalent Organic Framework as an All-Solid-State Lithium-Ion Battery Cathode with High Capacity. *Angew. Chem., Int. Ed.* **2020**, *59* (46), 20385−20389.
(21) Zhao, H.; Chen, H.; Xu, C.; Li, Z.; Ding, B.; Dou, H.; Zhang, X. Charge Storage Mechanism of an Anthraquinone-Derived Porous Covalent Organic Framework with Multiredox Sites as Anode Material for Lithium-Ion Battery. *ACS Appl. Energy Mater.* **2021**, *4* (10), 11377−11385.
(22) Shehab, M. K.; Weeraratne, K. S.; Huang, T.; Lao, K. U.; El-Kaderi, H. M. Exceptional Sodium-Ion Storage by an Aza-Covalent Organic Framework for High Energy and Power Density Sodium-Ion Batteries. *ACS Appl. Mater. Interfaces* **2021**, *13* (13), 15083−15091.
(23) Zhu, D.; Xu, G.; Barnes, M.; Li, Y.; Tseng, C.; Zhang, Z.; Zhang, J.; Zhu, Y.; Khalil, S.; Rahman, M. M.; Verduzco, R.; Ajayan, P. M. Covalent Organic Frameworks for Batteries. *Adv. Funct. Mater.* **2021**, *31* (32), 2100505.
(24) Hu, Y.; Wayment, L. J.; Haslam, C.; Yang, X.; Lee, S.; Jin, Y.; Zhang, W. Covalent Organic Framework Based Lithium-Ion Battery: Fundamental, Design and Characterization. *EnergyChem* **2021**, *3* (1), 100048.
(25) Park, J. H.; Kwak, M.; Hwang, C.; Kang, K.; Liu, N.; Jang, J.; Grzybowski, B. A. Self-Assembling Films of Covalent Organic Frameworks Enable Long-Term, Efficient Cycling of Zinc-Ion Batteries. *Adv. Mater.* **2021**, *33* (34), 2101726.
(26) Haldar, S.; Schneemann, A.; Kaskel, S. Covalent Organic Frameworks as Model Materials for Fundamental and Mechanistic Understanding of Organic Battery Design Principles. *J. Am. Chem. Soc.* **2023**, *145* (25), 13494−13513.
(27) Wang, M.; Wang, G.; Naisa, C.; Fu, Y.; Gali, S. M.; Paasch, S.; Wang, M.; Wittkaemper, H.; Papp, C.; Brunner, E.; et al. Poly-(Benzimidazobenzophenanthroline)-Ladder-Type Two-Dimensional Conjugated Covalent Organic Framework for Fast Proton Storage. *Angew. Chem.* **2023**, *135*, No. e202310937.
(28) Sabaghi, D.; Wang, Z.; Bhauriyal, P.; Lu, Q.; Morag, A.; Mikhailovia, D.; Hashemi, P.; Li, D.; Neumann, C.; Liao, Z.; Dominic, A. M.; Nia, A. S.; Dong, R.; Zschech, E.; Turchanin, A.; Heine, T.; Yu, M.; Feng, X. Ultrathin Positively Charged Electrode Skin for Durable Anion-Intercalation Battery Chemistries. *Nat. Commun.* **2023**, *14* (1), 760.
(29) Wang, H.; Zhai, Y.; Li, Y.; Cao, Y.; Shi, B.; Li, R.; Zhu, Z.; Jiang, H.; Guo, Z.; Wang, M.; Chen, L.; Liu, Y.; Zhou, K.-G.; Pan, F.; Jiang, Z. Covalent Organic Framework Membranes for Efficient Separation of Monovalent Cations. *Nat. Commun.* **2022**, *13* (1), 7123.
(30) Singh, R.; Kim, D. High-Temperature Proton Conduction in Covalent Organic Frameworks Interconnected with Nanochannels for Reverse Electrodialysis. *ACS Appl. Mater. Interfaces* **2021**, *13* (28), 33437−33448.
(31) Chen, S.; Zhu, C.; Xian, W.; Liu, X.; Liu, X.; Zhang, Q.; Ma, S.; Sun, Q. Imparting Ion Selectivity to Covalent Organic Framework Membranes Using de Novo Assembly for Blue Energy Harvesting. *J. Am. Chem. Soc.* **2021**, *143* (25), 9415−9422.
(32) Man, Z.; Safaei, J.; Zhang, Z.; Wang, Y.; Zhou, D.; Li, P.; Zhang, X.; Jiang, L.; Wang, G. Serosa-Mimetic Nanoarchitecture Membranes for Highly Efficient Osmotic Energy Generation. *J. Am. Chem. Soc.* **2021**, *143* (39), 16206−16216.
(33) Singh, R.; Kim, D. Ultrafast Ion-Transport at Hierarchically Porous Covalent-Organic Membrane Interface for Efficient Power Production. *Nano Energy* **2022**, *92*, 106690.
(34) Zhu, C.; Xian, W.; Song, Y.; Zuo, X.; Wang, Y.; Ma, S.; Sun, Q. Manipulating Charge Density in Nanofluidic Membranes for Optimal Osmotic Energy Production Density. *Adv. Funct. Mater.* **2022**, *32* (9), 2109210.
(35) Xin, W.; Zhang, Z.; Huang, X.; Hu, Y.; Zhou, T.; Zhu, C.; Kong, X.-Y.; Jiang, L.; Wen, L. High-Performance Silk-Based Hybrid Membranes Employed for Osmotic Energy Conversion. *Nat. Commun.* **2019**, *10* (1), 3876.
(36) Pattle, R. E. Production of Electric Power by Mixing Fresh and Salt Water in the Hydroelectric Pile. *Nature* **1954**, *174* (4431), 660−660.
(37) Ramon, G. Z.; Feinberg, B. J.; Hoek, E. M. V. Membrane-Based Production of Salinity-Gradient Power. *Energy Environ. Sci.* **2011**, *4* (11), 4423.
(38) Kim, D.-K.; Duan, C.; Chen, Y.-F.; Majumdar, A. Power Generation from Concentration Gradient by Reverse Electrodialysis in Ion-Selective Nanochannels. *Microfluid. Nanofluid.* **2010**, *9* (6), 1215−1224.
(39) Ji, J.; Kang, Q.; Zhou, Y.; Feng, Y.; Chen, X.; Yuan, J.; Guo, W.; Wei, Y.; Jiang, L. Osmotic Power Generation with Positively and Negatively Charged 2D Nanofluidic Membrane Pairs. *Adv. Funct. Mater.* **2017**, *27* (2), 1603623.
(40) Zhang, Z.; Shen, W.; Lin, L.; Wang, M.; Li, N.; Zheng, Z.; Liu, F.; Cao, L. Vertically Transported Graphene Oxide for High-Performance Osmotic Energy Conversion. *Adv. Sci.* **2020**, *7* (12), 2000286.
(41) Zhu, C.; Liu, P.; Niu, B.; Liu, Y.; Xin, W.; Chen, W.; Kong, X.-Y.; Zhang, Z.; Jiang, L.; Wen, L. Metallic Two-Dimensional MoS 2 Composites as High-Performance Osmotic Energy Conversion Membranes. *J. Am. Chem. Soc.* **2021**, *143* (4), 1932−1940.
(42) Zhang, Z.; Yang, S.; Zhang, P.; Zhang, J.; Chen, G.; Feng, X. Mechanically Strong MXene/Kevlar Nanofiber Composite Mem-

https://doi.org/10.1021/acs.jpcb.6c01511
J. Phys. Chem. B 2026, 130, 5775−5790

branes as High-Performance Nanofluidic Osmotic Power Generators. *Nat. Commun.* **2019**, *10* (1), 2920.
(43) Hong, S.; Ming, F.; Shi, Y.; Li, R.; Kim, I. S.; Tang, C. Y.; Alshareef, H. N.; Wang, P. Two-Dimensional Ti 3 C 2 T x MXene Membranes as Nanofluidic Osmotic Power Generators. *ACS Nano* **2019**, *13* (8), 8917−8925.
(44) Yang, G.; Liu, D.; Chen, C.; Qian, Y.; Su, Y.; Qin, S.; Zhang, L.; Wang, X.; Sun, L.; Lei, W. Stable Ti 3 C 2 T x MXene−Boron Nitride Membranes with Low Internal Resistance for Enhanced Salinity Gradient Energy Harvesting. *ACS Nano* **2021**, *15* (4), 6594−6603.
(45) Koltonow, A. R.; Huang, J. Two-Dimensional Nanofluidics. *Science* **2016**, *351* (6280), 1395−1396.
(46) Xin, W.; Jiang, L.; Wen, L. Two-Dimensional Nanofluidic Membranes toward Harvesting Salinity Gradient Power. *Acc. Chem. Res.* **2021**, *54* (22), 4154−4165.
(47) Fan, H.; Mundstock, A.; Feldhoff, A.; Knebel, A.; Gu, J.; Meng, H.; Caro, J. Covalent Organic Framework−Covalent Organic Framework Bilayer Membranes for Highly Selective Gas Separation. *J. Am. Chem. Soc.* **2018**, *140* (32), 10094−10098.
(48) Cao, L.; Liu, X.; Shinde, D. B.; Chen, C.; Chen, I.-C.; Li, Z.; Zhou, Z.; Yang, Z.; Han, Y.; Lai, Z. Oriented Two-Dimensional Covalent Organic Framework Membranes with High Ion Flux and Smart Gating Nanofluidic Transport. *Angew. Chem., Int. Ed.* **2022**, *61* (6), No. e202113141.
(49) Sheng, F.; Wu, B.; Li, X.; Xu, T.; Shehzad, M. A.; Wang, X.; Ge, L.; Wang, H.; Xu, T. Efficient Ion Sieving in Covalent Organic Framework Membranes with Sub-2-Nanometer Channels. *Adv. Mater.* **2021**, *33* (44), 2104404.
(50) Bing, S.; Xian, W.; Chen, S.; Song, Y.; Hou, L.; Liu, X.; Ma, S.; Sun, Q.; Zhang, L. Bio-Inspired Construction of Ion Conductive Pathway in Covalent Organic Framework Membranes for Efficient Lithium Extraction. *Matter* **2021**, *4* (6), 2027−2038.
(51) Zhang, P.; Chen, S.; Zhu, C.; Hou, L.; Xian, W.; Zuo, X.; Zhang, Q.; Zhang, L.; Ma, S.; Sun, Q. Covalent Organic Framework Nanofluidic Membrane as a Platform for Highly Sensitive Bionic Thermosensation. *Nat. Commun.* **2021**, *12* (1), 1844.
(52) Zhao, S.; Jiang, C.; Fan, J.; Hong, S.; Mei, P.; Yao, R.; Liu, Y.; Zhang, S.; Li, H.; Zhang, H.; Sun, C.; Guo, Z.; Shao, P.; Zhu, Y.; Zhang, J.; Guo, L.; Ma, Y.; Zhang, J.; Feng, X.; Wang, F.; Wu, H.; Wang, B. Hydrophilicity Gradient in Covalent Organic Frameworks for Membrane Distillation. *Nat. Mater.* **2021**, *20* (11), 1551−1558.
(53) Li, Y.; Wu, Q.; Guo, X.; Zhang, M.; Chen, B.; Wei, G.; Li, X.; Li, X.; Li, S.; Ma, L. Laminated Self-Standing Covalent Organic Framework Membrane with Uniformly Distributed Subnanopores for Ionic and Molecular Sieving. *Nat. Commun.* **2020**, *11* (1), 599.
(54) Cao, L.; Chen, I.-C.; Chen, C.; Shinde, D. B.; Liu, X.; Li, Z.; Zhou, Z.; Zhang, Y.; Han, Y.; Lai, Z. Giant Osmotic Energy Conversion through Vertical-Aligned Ion-Permselective Nanochannels in Covalent Organic Framework Membranes. *J. Am. Chem. Soc.* **2022**, *144* (27), 12400−12409.
(55) Liu, X.; He, M.; Calvani, D.; Qi, H.; Gupta, K. B. S. S.; de Groot, H. J. M.; Sevink, G. J. A.; Buda, F.; Kaiser, U.; Schneider, G. F. Power Generation by Reverse Electrodialysis in a Single-Layer Nanoporous Membrane Made from Core−Rim Polycyclic Aromatic Hydrocarbons. *Nat. Nanotechnol.* **2020**, *15* (4), 307−312.
(56) Feng, J.; Graf, M.; Liu, K.; Ovchinnikov, D.; Dumcenco, D.; Heiranian, M.; Nandigana, V.; Aluru, N. R.; Kis, A.; Radenovic, A. Single-Layer MoS2 Nanopores as Nanopower Generators. *Nature* **2016**, *536* (7615), 197−200.
(57) Li, C.; Wen, L.; Sui, X.; Cheng, Y.; Gao, L.; Jiang, L. Large-Scale, Robust Mushroom-Shaped Nanochannel Array Membrane for Ultrahigh Osmotic Energy Conversion. *Sci. Adv.* **2021**, *7* (21), No. eabg2183.
(58) Liao, D.; Xu, Z.; Wei, M.; Wang, Y. Interference Mechanism of Cations on Transport of Lithium and Magnesium inside COF Nanofiltration Membranes. *Mol. Simul.* **2022**, *48* (15), 1369−1377.
(59) Lyu, B.; Wang, M.; Jiang, Z.; Jiang, J. Microscopic Insight into Anion Conduction in Covalent−organic Framework Membranes: A Molecular Simulation Study. *J. Membr. Sci.* **2022**, *658*, 120754.
(60) Wei, M.; Zhou, W.; Xu, F.; Wang, Y. Nanofluidic Behaviors of Water and Ions in Covalent Triazine Framework (CTF) Multilayers. *Small* **2020**, *16* (9), 1903879.
(61) Xu, F.; Wei, M.; Zhang, X.; Wang, Y. Effect of Hydrophilicity on Water Transport through Sub-Nanometer Pores. *J. Membr. Sci.* **2020**, *611*, 118297.
(62) Ozcan, A.; Perego, C.; Salvalaglio, M.; Parrinello, M.; Yazaydin, O. Concentration Gradient Driven Molecular Dynamics: A New Method for Simulations of Membrane Permeation and Separation. *Chem. Sci.* **2017**, *8* (5), 3858−3865.
(63) Meng, B.; Liu, J.; Wang, L. Oligo(Ethylene Glycol) as Side Chains of Conjugated Polymers for Optoelectronic Applications. *Polym. Chem.* **2020**, *11* (7), 1261−1270.
(64) Perdew, J. P.; Burke, K.; Ernzerhof, M. Generalized Gradient Approximation Made Simple. *Phys. Rev. Lett.* **1996**, *77* (18), 3865−3868.
(65) Kresse, G.; Joubert, D. From Ultrasoft Pseudopotentials to the Projector Augmented-Wave Method. *Phys. Rev. B* **1999**, *59* (3), 1758−1775.
(66) Grimme, S. Semiempirical GGA-Type Density Functional Constructed with a Long-Range Dispersion Correction. *J. Comput. Chem.* **2006**, *27* (15), 1787−1799.
(67) Feng, X.; Chen, L.; Honsho, Y.; Saengsawang, O.; Liu, L.; Wang, L.; Saeki, A.; Irle, S.; Seki, S.; Dong, Y.; Jiang, D. An Ambipolar Conducting Covalent Organic Framework with Self-Sorted and Periodic Electron Donor-Acceptor Ordering. *Adv. Mater.* **2012**, *24* (22), 3026−3031.
(68) Jin, S.; Supur, M.; Addicoat, M.; Furukawa, K.; Chen, L.; Nakamura, T.; Fukuzumi, S.; Irle, S.; Jiang, D. Creation of Superheterojunction Polymers via Direct Polycondensation: Segregated and Bicontinuous Donor−Acceptor π-Columnar Arrays in Covalent Organic Frameworks for Long-Lived Charge Separation. *J. Am. Chem. Soc.* **2015**, *137* (24), 7817−7827.
(69) Thomas, S.; Li, H.; Zhong, C.; Matsumoto, M.; Dichtel, W. R.; Bredas, J.-L. Electronic Structure of Two-Dimensional π-Conjugated Covalent Organic Frameworks. *Chem. Mater.* **2019**, *31* (9), 3051−3065.
(70) Lukose, B.; Kuc, A.; Frenzel, J.; Heine, T. On the Reticular Construction Concept of Covalent Organic Frameworks. *Beilstein J. Nanotechnol.* **2010**, *1*, 60−70.
(71) Koo, B. T.; Dichtel, W. R.; Clancy, P. A Classification Scheme for the Stacking of Two-Dimensional Boronate Ester-Linked Covalent Organic Frameworks. *J. Mater. Chem.* **2012**, *22* (34), 17460.
(72) Wang, L.; Dong, B.; Ge, R.; Jiang, F.; Xu, J. Fluorene-Based Two-Dimensional Covalent Organic Framework with Thermoelectric Properties through Doping. *ACS Appl. Mater. Interfaces* **2017**, *9* (8), 7108−7114.
(73) He, Y.; Yang, S.; Fu, Y.; Wang, F.; Ma, J.; Wang, G.; Chen, G.; Wang, M.; Dong, R.; Zhang, P.; Feng, X. Electronic Doping of Metal-Organic Frameworks for High-Performance Flexible Micro-Supercapacitors. *Small Struct.* **2021**, *2* (3), 2000095.
(74) Zhu, P.; Meunier, V. Electronic Properties of Two-Dimensional Covalent Organic Frameworks. *J. Chem. Phys.* **2012**, *137* (24), 244703.
(75) Adjizian, J.-J.; Briddon, P.; Humbert, B.; Duvail, J.-L.; Wagner, P.; Adda, C.; Ewels, C. Dirac Cones in Two-Dimensional Conjugated Polymer Networks. *Nat. Commun.* **2014**, *5* (1), 5842.
(76) Gutzler, R.; Perepichka, D. F. π-Electron Conjugation in Two Dimensions. *J. Am. Chem. Soc.* **2013**, *135* (44), 16585−16594.
(77) Gutzler, R. Band-Structure Engineering in Conjugated 2D Polymers. *Phys. Chem. Chem. Phys.* **2016**, *18* (42), 29092−29100.
(78) Manz, T. A.; Limas, N. G. Introducing DDEC6 Atomic Population Analysis: Part 1. Charge Partitioning Theory and Methodology. *RSC Adv.* **2016**, *6* (53), 47771−47801.
(79) Limas, N. G.; Manz, T. A. Introducing DDEC6 Atomic Population Analysis: Part 2. Computed Results for a Wide Range of Periodic and Nonperiodic Materials. *RSC Adv.* **2016**, *6* (51), 45727−45747.

https://doi.org/10.1021/acs.jpcb.6c01511
J. Phys. Chem. B 2026, 130, 5775−5790

(80) Manz, T. A. Introducing DDEC6 Atomic Population Analysis: Part 3. Comprehensive Method to Compute Bond Orders. *RSC Adv.* **2017**, *7* (72), 45552−45581.
(81) Limas, N. G.; Manz, T. A. Introducing DDEC6 Atomic Population Analysis: Part 4. Efficient Parallel Computation of Net Atomic Charges, Atomic Spin Moments, Bond Orders, and More. *RSC Adv.* **2018**, *8* (5), 2678−2707.
(82) Mayo, S. L.; Olafson, B. D.; Goddard, W. A. DREIDING: A Generic Force Field for Molecular Simulations. *J. Phys. Chem.* **1990**, *94* (26), 8897−8909.
(83) Rawat, K. S.; Borgmans, S.; Braeckevelt, T.; Stevens, C. V.; Van Der Voort, P.; Van Speybroeck, V. How the Layer Alignment in Two-Dimensional Nanoporous Covalent Organic Frameworks Impacts Its Electronic Properties. *ACS Appl. Nano Mater.* **2022**, *5* (10), 14377−14387.
(84) Thompson, A. P.; Aktulga, H. M.; Berger, R.; Bolintineanu, D. S.; Brown, W. M.; Crozier, P. S.; in't Veld, P. J.; Kohlmeyer, A.; Moore, S. G.; Nguyen, T. D.; Shan, R.; Stevens, M. J.; Tranchida, J.; Trott, C.; Plimpton, S. J. LAMMPS - a Flexible Simulation Tool for Particle-Based Materials Modeling at the Atomic, Meso, and Continuum Scales. *Comput. Phys. Commun.* **2022**, *271*, 108171.
(85) Fyta, M.; Netz, R. R. Ionic Force Field Optimization Based on Single-Ion and Ion-Pair Solvation Properties: Going beyond Standard Mixing Rules. *J. Chem. Phys.* **2012**, *136* (12), 124103.
(86) Bonthuis, D. J.; Mamatkulov, S. I.; Netz, R. R. Optimization of Classical Nonpolarizable Force Fields for OH − and H 3 O +. *J. Chem. Phys.* **2016**, *144* (10), 104503.
(87) Dočkal, J.; Moučka, F.; Lísal, M. Molecular Dynamics of Graphene−Electrolyte Interface: Interfacial Solution Structure and Molecular Diffusion. *J. Phys. Chem. C* **2019**, *123* (43), 26379−26396.
(88) Solano, C. J. F.; Jeremias, S.; Paillard, E.; Beljonne, D.; Lazzaroni, R. A Joint Theoretical/Experimental Study of the Structure, Dynamics, and Li + Transport in Bis([Tri]Fluoro-[Methane]Sulfonyl)Imide [T]FSI-Based Ionic Liquids. *J. Chem. Phys.* **2013**, *139* (3), 034502.
(89) Fong, K. D.; Self, J.; Diederichsen, K. M.; Wood, B. M.; McCloskey, B. D.; Persson, K. A. Ion Transport and the True Transference Number in Nonaqueous Polyelectrolyte Solutions for Lithium Ion Batteries. *ACS Cent. Sci.* **2019**, *5* (7), 1250−1260.
(90) Apel, P. Y.; Biesheuvel, P. M.; Bobreshova, O. V.; Borisov, I. L.; Vasil'eva, V. I.; Volkov, V. V.; Grushevenko, E. A.; Nikonenko, V. V.; Parshina, A. V.; Pismenskaya, N. D.; Ryzhkov, I. I.; Sharafan, M. V.; Yaroslavtsev, A. B. Concentration Polarization in Membrane Systems. *Membr. Membr. Technol.* **2024**, *6* (3), 133−161.
(91) Ahmad, M.; Ahmed, M. Characterization and Applications of Ion-Exchange Membranes and Selective Ion Transport through Them: A Review. *J. Appl. Electrochem.* **2023**, *53* (8), 1537−1562.

https://doi.org/10.1021/acs.jpcb.6c01511
J. Phys. Chem. B 2026, 130, 5775−5790